Master Thesis

Electrical actuation and frequency tuning of 2D mechanical resonators

Jaap van Dorp

Technische Universiteit Delft

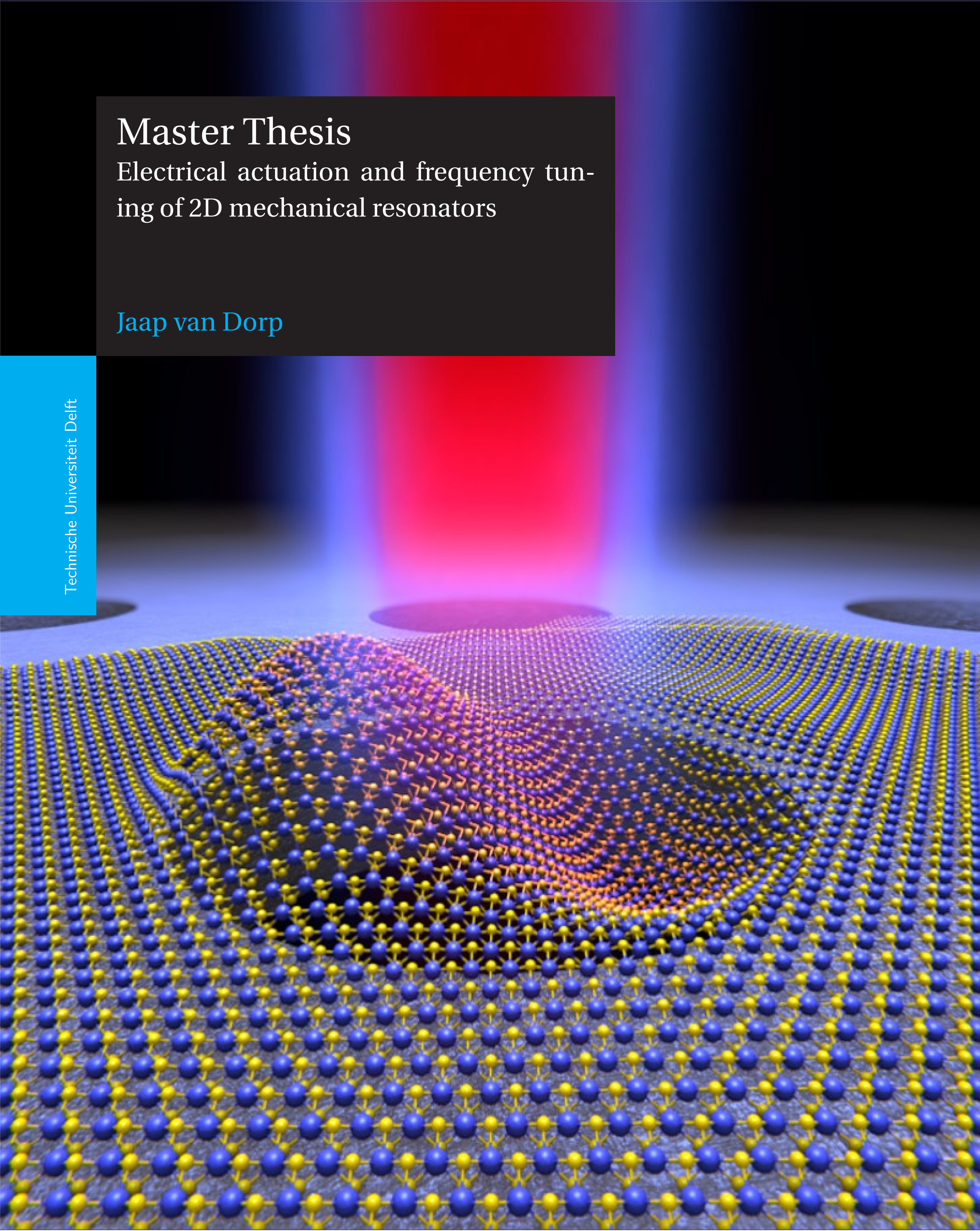

TU Delft Delft University of Technology

Challenge the future

Master Thesis

Electrical actuation and frequency tuning of 2D mechanical resonators

by

Jaap van Dorp

in partial fulfillment of the requirements for the degree of

Master of Science
in Applied Physics

at the Delft University of Technology,
to be defended publicly on Thursday April 2, 2015 at 11:45 AM.

Student number:	1516477	
Project duration:	September 1, 2013 – April 2, 2015	
Supervisor:	Prof. dr. ir. H.S.J. van der Zant	
Thesis committee:	Prof. dr. ir. H.S.J. van der Zant,	TU Delft
	Prof. dr. P.G. Steeneken,	TU Delft
	Prof. dr. Y.M. Blanter,	TU Delft

An electronic version of this thesis is available at http://repository.tudelft.nl/.

The MoS_2 resonator image on the cover is taken from an inside cover of Advanced Materials, volume 25, 2013.

Abstract

The electrical actuation of suspended membrane nanomechanical resonators incorporated into a laser interferometer displacement setup was investigated. Graphene and MoS2 membranes have been used to show electrical actuation of both metals and semiconductors. The method to fabricate devices was optimized and the properties of the fabricated devices are documented in order to make future device farication easier when specific properties are required.

The first experiment performed with the electrical actuation was done in order to investigate the frequency tuning the of the 2D resonators. Resonance frequencies in the range of 15-55 MHz are observed without frequency tuning, where variations are due to differences in diameter and thickness of the suspended drums and the built-in tension. Applying a DC voltage caused both a decrease and an increase in the resonance frequency, depending on the device and the magnitude of the voltage. A maximum (increasing) frequency tuning sensitivity of 7.62 MHz/V was achieved.

Furthermore, the model of interactions in 2D circular membrane due to electric actuation and DC gate voltage tuning in the linear resonator regime is compared to the measurement results. This comparison gives insight in the interaction between electrostatic spring softening and mechanically induced strain in membranes with different properties. The investigated model was insufficient to explain the measured frequency changes due to the applied DC voltages.

ACKNOWLEDGEMENT

Naturally, I would like to thank everyone at the Molecular Electronics and Devices group at the TU Delft. They are a group of academics who enjoy doing science and it shows. Everybody is enthusiastic about their research projects and were always interested in what I was doing. I enjoyed spending time talking about research, day-to-day topics and how to best make an espresso. Also coming up with the words of the day and enjoying social events with you all is a fond memory for me. Regarding my project making mechanical resonators, I would like to thank Ronald, my supervisor, for his allround guidance. Whether I needed help with a theoretical explanation, a setup adjustment, a software problem or training in the clean room and on other tools, he was there to teach me. Next, I want to thank Warner for his supervision when Ronald was not available (because even Ronald needs a holiday sometimes). His enthusiasm for experiments is amazing and he stimulated me to think deeper about the experiments I did and how to explain the phenomena that my measurements showed. Also worthy of my thanks are Santiago and Dejan, who were always enthusiastic about my experiments and were willing to assist wherever possible. They made me feel like a peer and even wanted me to teach them what I had already learned about the interferometer setup and sample fabrication when they joined MED shortly after I did.

At the TU Delft, a master thesis is supposed to last for 9 months. It took me 19 months to finish the experiments and thesis... One of the main reasons for this delay is that besides a university degree, I also pursue the goal to become an Olympian in my favourite sport: curling. In order to balance both these challenging tasks, there is very little room for error in planning a time schedule. Setting the right priorities is crucial and even with my experience in planning and knowledge of my own time-equation if you will, it goes wrong occasionally. Sometimes curling was the most important and I was not at the university and mostly from september 2014-november 2014, writing my thesis was not my main focus. Therefore, I would like to apologize to all those involved at TU Delft for the difficulties this has caused them and I would like to thank everyone for being understanding and supportive. Especially Ronald has truly been a source of inspiration when it comes to patience. I was not an easy student to supervise, but he managed to guide me in the right direction and he always kept the discussions we had constructive.

Looking at the other side of my time-equation, I also owe my gratitude to my teammates, coach and parents. My teammates and coach have adjusted the time for practice when I was not able to make it on time in the evenings, have supported me in writing my thesis even while away on tournaments and have showed interest in a topic that would otherwise not interest them. They have also accepted me ditching practice or sessions at the gym when I was finishing my thesis.

And finally, most importantly, balancing my time-equation: my parents. They have supported me in every way they could, making it possible for me to follow my dreams. They motivate me by asking the right questions, saying the right things or simply knowing when not to say anything.

This project has grown to be much more than a part of the curriculum for me. I acquired academic knowledge about a scientific subject and developed numerous skills working in the clean room and experimenting on the interferometer setup and on the AFM. I also expanded my writing and documentating experience and developed a better understanding of how to plan and execute the parts of a project that don't excite me as much as experimenting. All that is left is for me to hope that you enjoy reading my thesis as much as I have enjoyed travelling the road towards its completion.

CONTENTS

1
INTRODUCTION

In the past decades, the technological progress in electronics has been gigantic. Smartphones have taken over the use of many electronic devices such as digital (video) cameras, GPS navigation systems, clocks/watches, calculators, handheld gaming devices, radios and music playing devices. As devices become more complex, a big topic of neccesary development is the scaling down of transistors. Moore's law initially predicted in 1965 that the size of a transistor would be halved every year [1]. This statement was adjusted ten years later to say transistors will be halved in size every two years, which is still a rather accurate prediction up to date. Smaller transistors means an increase in the calculation capacity due to an increased number of transistors that can be placed on a chip. The power each of these computer chip components dissipates scales down with its size, another important aspect of todays technology. These developments have not only brought the possibility of more calculations per second, but have inspired a scaling down of many more aspects of technology.

When looking at a slightly broader perspective, the decrease in transistor size over the last decades has allowed for the transistion from Microelectromechanical systems (MEMS) to Nanoelectromechanical systems (NEMS). NEMS are defined as a class of devices integrating functionality of electrical and mechanical functionality on the nanoscale.

Since the discovery of graphene, a sheet of a single atomic layer of graphite [2], much research has been done on the properties of graphene and other two dimensional materials (2D materials) [3–13]. Since exfoliation is possible on a vast range of bulk materials to obtain 2D materials, combinations of studies are possible on metals, such as graphene, semiconductors (e.g. molybdenum disulfide) and insulators (e.g. hexagonal boron nitride).

These 2D materials are interesting for research because they show different properties from their bulk versions. The optical transparency [14], optomechanical properties [15, 16], and most importantly for this thesis, interesting electrical [2, 17, 18] and superior mechanical [4, 7, 11, 19] properties provide an important reason for the investigation of the possibilities of the integration of these materials in current semiconductor and MEMS technology.

The incorporation of 2D materials into MEMS and NEMS technology is mostly focussed on sensor applications. Nanomechanical resonators are formed by freely suspended devices that can be thinned down to a single layer of material. These devices providing the ultimate surface-to-volume ratio and thus the lower limit in mass. Due to the high elastic modulus [10, 20], the resonators also maintain a high resonance frequency. With frequencies from the kHz to the GHz range, mechanical resonators made from 2D materials have a broad variety of application.

The main research goal of this thesis project is to develop a fabrication method for 2D mechanical resonators that can be actuated electrically and to successfully measure the electrically driven resonance frequencies of these resonators in the current interferometer setup. The secondary goal is to develop a better understanding of the frequency tuning possibilities of these devices.

2

THEORY

2.1. RESONATORS

A resonator is defined as a driven oscillator. A system which moves with a certain fundamental frequency without external forces acting on it is an oscillator, while a resonator requires an external force, or actuation, to initiate and maintain the motion at a specific frequency.

2.1.1. HARMONIC OSCILLATOR

The behaviour of a resonator can be modelled by the equations of motion of a mass-spring system. A mass-spring system is in equillibrium when no external forces are applied, but when the mass is displaced, the spring will cause it to return to the equilibrium position, starting an oscillation with frequency $\omega_0 = \sqrt{\frac{k}{m}}$ when no friction is involved. However, it is more realistic that there is a certain damping that reduces the amplitude of the oscillation until the mass is stationary in its equilibrium position again. In order to describe the mechanical resonator system examined in this thesis, it is interesting to first look at the general equation for a damped harmonic oscillator.

$$
\begin{aligned}
m\frac{d^2u(t)}{dt^2} + m\eta\frac{du(t)}{dt} + ku(t) = 0 \\
\frac{d^2u(t)}{dt^2} + \eta\frac{du(t)}{dt} + \omega_0^2 u(t) = 0
\end{aligned} \tag{2.1}
$$

Where m is the mass, $u(t)$ is the mass displacement, η is the velocity proportional damping factor and k is the spring constant. A solution to this equation is the following complex function.

$$u(t) = a_0 \mathrm{e}^{i\omega t} \tag{2.2}$$

By substituting this solution into equation 2.1 this gives

$$-\omega^2 + \eta i\omega + \omega_0^2 = 0 \tag{2.3}$$

And solving for ω gives

$$\omega = \frac{i\eta}{2} \pm \omega_0\sqrt{1 - \frac{\eta^2}{4\omega_0^2}} \tag{2.4}$$

The solution for ω substituted into equation 2.2 provide the following real and positive solution to equation 2.1

$$|u(t)| = |a_0 \mathrm{e}^{i\omega t}| = a_0 \mathrm{e}^{-\frac{\eta t}{2}} cos(\omega t) \tag{2.5}$$

The damping η is then rewritten by

$$\eta = \frac{\omega_0}{Q} \tag{2.6}$$

To simplify equation 2.5 to

$$u(t) = a_0 e^{-\frac{\omega_0 t}{2Q}} cos(\omega t) \tag{2.7}$$

Q-factor A measure of determining the quality of a resonator is the quality factor, or Q-factor, as seen in equation 2.6. This dimensionless parameter defines the energy stored in the system divided by the energy dissipated per cycle. Another way of expressing this parameter is determining the ratio between the bandwidth of a resonator signal and the resonance frequency, as expressed by equation 2.8. This is how the Q-factor will be determined experimentally.

$$Q = \frac{f_{res}}{\Delta f} \tag{2.8}$$

Where f_{res} is the resonance frequency and Δf represents the bandwidth. The bandwidth is measured as the full-width-at-half-maximum (FWHM) of the resonance peak, meaning the width of the peak (in Hz) is measured at half the peak height ($\frac{maximum \quad amplitude \quad - \quad minimum \quad amplitude}{2}$). The Q-factor as defined in equation 2.8 is often more specifically defined as the spectral Q-factor (from here on refered to as the spectral Q), since it provides the quality of the determination of the membrane motion using a spectrum measurement. While the spectral Q is a simple measure of the quality of the resonator, several dissipative mechanisms influence the noise of a resonance measurement.

In order to maintain a constant resonance, a system is often driven by an external force $F_0 e^{i\omega t}$, or the real form $F_0 cos(\omega t)$. Adding this to equation 2.1 and rewriting is gives the following equation.

$$\frac{d^2u(t)}{dt^2} + \eta\frac{du(t)}{dt} + \omega_0^2 u(t) = \frac{F_0 cos(\omega t)}{m} \tag{2.9}$$

Equation 2.9 has a homogeneous solution, which has already been shown above. The particular solution is of the form

$$u(t) = Re(Ce^{i\omega t}) \tag{2.10}$$

The real driving force $F_0 cos(\omega t)$ has the complex form $F_0 e^{i\omega t}$. Substituting this and the solution 2.10 into equation 2.9 gives

$$-\omega^2 Ce^{i\omega t} + \frac{\omega_0}{Q} i\omega Ce^{i\omega t} + \omega^2 Ce^{i\omega t} = \frac{F_0}{m} e^{i\omega t} \tag{2.11}$$

Further simplifying this, an expression for the complex function C is obtained.

$$C = \frac{\frac{F_0}{m}}{-\omega^2 + \frac{\omega_0}{Q} i\omega + \omega_0^2} \tag{2.12}$$

When writing equation 2.12 in the complex form $C = c_0(\omega)e^{i\phi}$, we obtain the magnitude lineshape the harmonic oscillator will show in the frequency domain and the accompanying phase.

$$\begin{aligned} c_0(\omega) = C\bar{C} &= \frac{\frac{F_0}{m}}{\sqrt{(\omega_0^2 - \omega^2)^2 + (\frac{\omega_0}{Q}\omega)^2}} \\ \phi(\omega) = arg(C) &= \begin{cases} arctan(\frac{\omega\omega_0}{Q(\omega^2\omega_0^2)}) & \omega < \omega_0 \\ arctan(\frac{\omega\omega_0}{Q(\omega^2\omega_0^2)}) + \pi & \omega > \omega_0 \end{cases} \end{aligned} \tag{2.13}$$

Plotting these solutions, an expectation can be formed of the data obtained in the experiments done during this thesis.

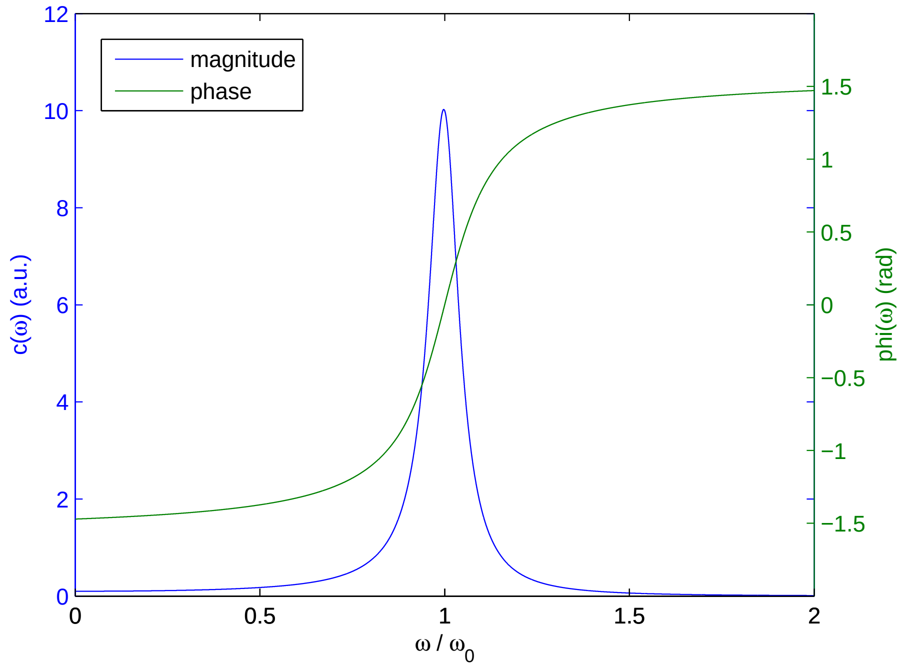

Figure 2.1.1: The graphs of equation 2.13, where the magnitude and phase are plotted against the normalized frequency as expected by the theory.

2.2. ACTUATION METHODS

Different means of actuating the membrane motion are possible, for instance optical [21, 22], electrostatic [5, 23, 24] magnetomotive [25, 26] , piezoelectric [27, 28] and piezoresistive [29, 30]. During the course of this thesis, the change from optical actuation to electrostatical actuation is made, which will be explained in more detail below.

During the course of this thesis, resonators are only actuated in the linear regime. This way the behaviour of a suspended drum can be easily modelled and the influence of the electrical actuation and frequency tuning explained 2.3 can be investigated. To assure that the resonators are driven in the linear regime, the driving power remains quite low, resulting in a small resonator amplitude.

Before looking at the actuation method used during this the experiments in this thesis, a more general understanding of the mechanical behaviour of a nanodrum is needed. The movement of the drum can be described by the Euler-Bernouilli equation, its general form is equation 2.14. Since a drum is symmetric around its center, the deflection is only dependent on the distance from the center, r. Since this is only one dimension, the 1D version of the Euler-Bernouilli equation is used.

$$\rho S\frac{\partial^2 u}{\partial t^2} + \eta\frac{\partial u}{\partial t} + EI\frac{\partial^4 u}{\partial x^4} - T\frac{\partial^2 u}{\partial x^2} = F \tag{2.14}$$

Where $u = u(x,t)$ is the displacement of the drum, ρ is the mass density, S is the cross section, η the damping, E is the young's modulus, I is the inertia, T is the tension and $F = F(x,t)$ is the external force. Simplifying this equation by first seperating the displacement into a static (time-independent) displacement and a dynamic displacement, so $u(x,t) = u_{dc}(x)u_{ac}(t)$. The static Euler-Bernouilli equation assumes a constant displacement as a function of time, or $u_{ac}(t) = c$, seen in the first line of the following equation. Also, the assumption is made that the driving force also consists of a static and dynamic component, or $F(x,t) = F_{ac}(x,t)F_{dc}(x)$. Equation 2.14 then gives two seperate equations:

$$\begin{aligned} EI\frac{\partial^4 u_{dc}(x)}{\partial x^4} - T\frac{\partial^2 u_{dc}(x)}{\partial x^2} = F_{dc}(x), u_{ac}(t) = c \\ \rho S\frac{\partial^2 u_{ac}}{\partial t^2} + \eta\frac{\partial u_{ac}}{\partial t} + EI\frac{\partial^4 u_{ac}}{\partial x^4} - T_{dc}\frac{\partial^2 u_{ac}}{\partial x^2} - T_{ac}\frac{\partial^2 u_{dc}}{\partial x^2} = F_{ac}(t) \end{aligned} \tag{2.15}$$

Where

$$\begin{aligned} T_{dc} &= T_0 + \frac{ES}{2l}\int_0^l \left(\frac{\partial u_{dc}}{\partial x}\right)^2 dx \\ T_{ac} &= \frac{ES}{l}\int_0^l \frac{\partial u_{dc}}{\partial x}\frac{\partial u_{ac}}{\partial x} dx \end{aligned} \tag{2.16}$$

When in the initial state, where a drum is not buckled, there is no change in displacement due as a function of position ($\frac{\partial u_{dc}}{\partial x} = 0$), so the dc tension term is reduced to $T_{dc} = T_0$. The small changes in displacement due to the actuation cause very little added tension in the drum, so we also assume $T_{ac} = 0$, meaning equation 2.15 becomes:

$$\begin{aligned} EI\frac{\partial^4 u_{dc}(x)}{\partial x^4} - T\frac{\partial^2 u_{dc}(x)}{\partial x^2} = F_{dc}(x) \\ \rho S\frac{\partial^2 u_{ac}}{\partial t^2} + \eta\frac{\partial u_{ac}}{\partial t} + EI\frac{\partial^4 u_{ac}}{\partial x^4} - T_0\frac{\partial^2 u_{ac}}{\partial x^2} = F_{ac}(t) \end{aligned} \tag{2.17}$$

Optical actuation Optical actuation is based on the periodic heating of the suspended membrane by the modulated intensity of a laser. Illuminating a drum with laser light that has an intensity modulated at a frequency equal to the resonance frequency of the drum causes the drum to expand and contract at that frequency.

Electrical actuation The principle of electrical actuation is based on the fact that the suspended membrane and a second conductive part of the sample form a capacitor. When grounding the sample and applying a voltage to the drum, a resulting electrostatic force causes the drum to deflect towards the bottom of the cavity. The expression for this force is given in equation 2.18.

$$\begin{aligned} F(x,t) = F_{el} &= \frac{1}{2}\frac{\partial C_g}{\partial u}(V_g^{dc})V_g^{ac} \\ F_{el}(x,t) &= \frac{1}{2}C_g[(V_g^{dc})^2 + 2V_g^{dc}V_g^{ac}cos(\omega t)] \\ F_{el}(x) &= \frac{1}{2}C_g(V_g^{dc})^2 \\ F_{el}(t) &= C_g V_g^{dc} V_g^{ac} cos(\omega t) \end{aligned} \tag{2.18}$$

Where F_{el} is the electrostatic force, C'_g is the derivative of the capacitance between the drum and gate and V_g^{dc} and V_g^{ac} are respectively the DC and time-varying RF voltages applied to the drum. The applied voltage on the drum is RF modulated so that the frequency of this AC-voltage corresponds to the resonance frequency of the drum, resulting in the drum moving at its resonance frequency. The approximation shows the simplified form of the actuation voltage when the position dependence of the capacitance between the drum and the gate is ignored. In other words, the assumption is made that the drum capacitance changes uniformly when the drum moves. It is known that this is not the case, but both position and time dependence of the actuation force will make the time-dependent Euler-Bernouilli equation difficult to solve. So combining the actuation force of equation 2.18 with the static and dynamic Euler-Bernouilli equation of 2.19, the following description is obtained:

$$
\begin{aligned}
&EI\frac{\partial^4 u_{dc}(x)}{\partial x^4} - T\frac{\partial^2 u_{dc}(x)}{\partial x^2} = \frac{1}{2}C_g(V_g^{dc})^2 \\
&\rho S\frac{\partial^2 u_{ac}}{\partial t^2} + \eta\frac{\partial u_{ac}}{\partial t} + EI\frac{\partial^4 u_{ac}}{\partial x^4} - T_0\frac{\partial^2 u_{ac}}{\partial x^2} = C_g V_g^{dc} V_g^{ac} cos(\omega t)
\end{aligned}
\tag{2.19}
$$

Figure 2.2.1 schematically shows the parameters of influence in the system and the mass spring system that can be used to simplify the system behaviour.

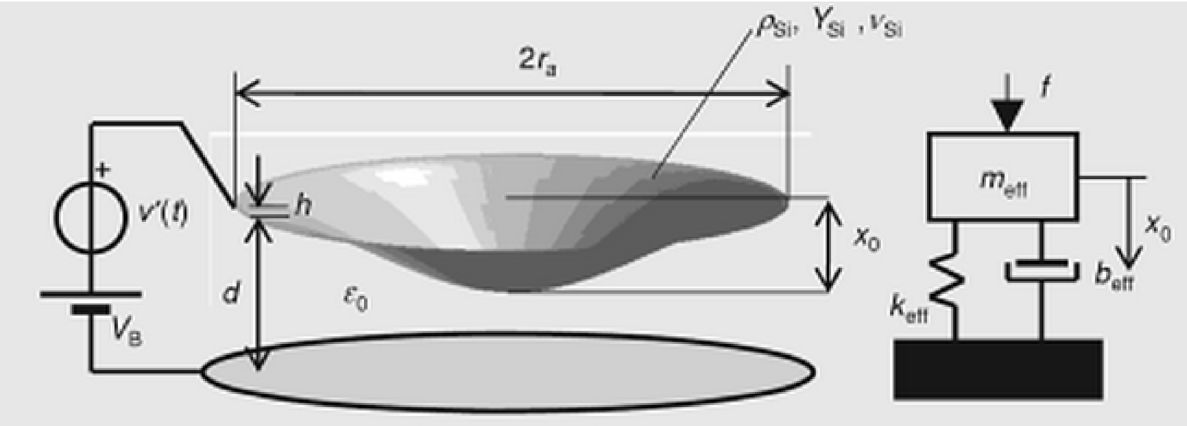

Figure 2.2.1: Schematic representation of a the suspended (silicon) membrane connected to a voltage source with $V_g^{dc} = V_B$ and $V_g^{ac} = v'(t)$. Further symbols describing this system are the thickness of the drum h, the radius r_a, the distance between drum and gate d, the deflection x_0, and the properties of the silicon: density ρ_{Si}, Young's modulus Y_{Si} and Poission ratio ν_{Si}. The behaviour of a suspended drum can be approximated by a mass-spring system with a certain damping (right figure). Here, the effective mass m, spring constant k and damping coefficient b (= η in equation 2.6) are resonating due to a driving force f. From Electromechanics and NEMS by Jones [31].

2.3. GATE TUNING DC SIGNAL

A DC voltage on the gate causes the membrane to deflect towards the sample [8]. Following the theory described by Changyao Chen in his Ph.D. thesis [12], the behaviour of fully clamped membranes with electrostatic forces acting on it will be described. Some excerpts from chapter 4.2 of his thesis will be discussed and further analysed to form an understanding of the systems behaviour and the equations that have been described in section 2.2. Note that the following quotations describe a systems containing graphene as a 2D material, but the equations hold for other 2D materials (with a range of certain conditions).

> **Chen Graphene NanoElectroMechanical Resonators and Oscillators p. 72**
> Similar to the doubly clamped case, we neglect the flexural rigidity of the suspended graphene, therefore treat it as a freestanding circular membrane clamped at the circumference. With the applied electrostatic force, the graphene will bend towards the gate, as shown in Figure 2.3.1. The mode shape $\xi(r)$ of such a deflected membrane under uniformly distributed force is given in [32], where the following function is found:
>
> $$\xi(r) = u_{dc}(1 - \frac{r^2}{R^2}) \tag{2.20}$$

The start of this theory is the static equation of 2.15. The assumption made in section 2.2 is that the static force F_{dc} is reduced to $F_{dc} = T_0$ in the pre-buckled state. However, the DC voltage that tunes the drum makes the external force $F_{dc} = \frac{ES}{2l}\int_0^l \left(\frac{\partial u_{dc}}{\partial x}\right)^2 dx$. The mode shape found in the above citation can be used for the displacement term. In order to simplify the model that describes the influence of the applied static force to the displacement and frequency behaviour of a drum, the first equation of 2.19 is reviewed in the energy domain. The following two citations provide a solution for the shape of the drum when statically deflected by a DC voltage, or in other words, when the drum is in its equilibrium position when under the influence of an external force.

For convience, we are using a polar coordinate system for drum resonators. Here, z is the deflection at the center of the drum, and R is the radius of the drum. The stored elastic energy (strain energy) U_{el} is [33]:

$$\begin{aligned} U_{el} &= \frac{\pi E t}{1-\nu_p^2}\int_0^R [\varepsilon_0 + \frac{1}{2}\xi'^2(r)]^2 r dr \\ &= \frac{\pi E t}{1-\nu_p^2}(\frac{2z^4}{3R^2} + \varepsilon z^2 + \frac{1}{2}\varepsilon^2 R^2), \end{aligned} \tag{2.21}$$

where t is the thickness of the graphene with the value of 3.5 Åand $Et = 340Nm^{-1}$, $\nu_p =$ 0.165 is Poisson's ratio, $\varepsilon'(r) = \frac{\partial \xi(r)}{\partial r}$.

An earlier assumption is then used, stating that the suspended membrane can be assumed to be a metallic plate over the gate electrode. The electrostatic energy of the desired capacitor can be expressed as follows:

$$U_{es} = -\frac{1}{2}C_g V_c^2 \tag{2.22}$$

Where C_g is the gate capacitance. Figure 2.3.1 shows how the suspended membrane is deflected towards the gate due to the electrostatic force. The general expression for the capacitance, $C_g = \frac{\varepsilon A}{d}$, where ε is the product of the electric constant and the dielectric constant, A is the surface of both plates and d is the distance between the two plates. Due to this dependence of the capacitance on the distance between the suspended membrane and the gate electrode, the deflection of the membrane due to the gate voltage changes the capacitance as a function of the radial distance from the drum center. The capacitance is therefore expanded in the three terms: $C_g \approx C_0 + C'z + C''z^2/2$, where $C' = dC_g/dz$ and $C'' = d^2C_g/dz^2$.

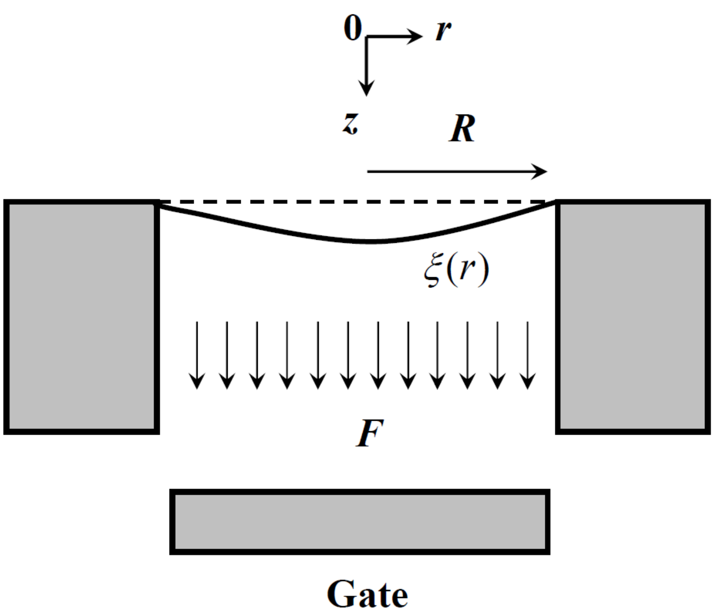

Figure 2.3.1: Mechanical model for fully clamped drum graphene with radius R under uniform force F, in polar coordinates. The equilibrium mode shape is described as $\xi(r)$. From Chen [12].

From this point onwards, Chen is followed again.

Chen Graphene NanoElectroMechanical Resonators and Oscillators p. 72-74

...to find the equilibrium position z_e, we set the total energy $U_{el} + U_{es}$ to minimum, namely:

$$\begin{aligned} \frac{8\pi Et}{3(1-\nu_p^2)R^2}z^3 + (\frac{2\pi Et\varepsilon_0}{1-\nu_p^2} - \frac{1}{2}C''V_g^2)z - \frac{1}{2}C'V_g^2 = 0 \\ \alpha' z^3 + \beta' z + \gamma' = 0 \end{aligned} \tag{2.23}$$

Where

$$\begin{aligned} \alpha' &= \frac{8\pi Et}{3(1-\nu_p^2)R^2} \\ \beta' &= \frac{2\pi Et\varepsilon_0}{1-\nu_p^2} - \frac{1}{2}C''V_g^2 \\ \gamma' &= -\frac{1}{2}C'V_g^2 \end{aligned} \tag{2.24}$$

...

The spring constant k of the graphene drum resonator is given as

$$k = \left.\frac{\partial^2(U_{el}+U_{es})}{\partial z^2}\right|_{z_e} = \frac{2\pi Et\varepsilon_0}{1-\nu_p^2} + \frac{8\pi Et}{(1-\nu_p^2)R^2}z_e^2 - \frac{1}{2}C''V_g^2 \tag{2.25}$$

After having found the expression for the spring constant at each gate voltage V_g, it is relatively straightforward to calculate the resonance frequency using equation 2.26.

$$f = \frac{1}{2\pi}\sqrt{\frac{k}{m_{eff}}} \tag{2.26}$$

By preforming the calculations described above, a resonance frequency (ω_0) profile as a function of the gate voltage (V_g) can be found for each device. The constants $E, t, \nu_p andR$ and the approximations for $C' andC''$ in equations 2.23, 2.24 and 2.25 are determined by the device geometry and properties. z_e is then calculated through equation 2.23. However, there are two free parameters determining the shape and values of the resonance frequency profile. They are the built-in strain ε_0 and the effective mass m_{eff}. These parameters are determined when fitting the acquired resonance frequency data with the model defined by Chen. When plotting the behaviour of the resonance frequency as a function of gate voltage described model for different built-in strain values ε_0, different types of behaviour occur. Although the effective mass m_{eff} also affects the behaviour, it is mostly a scaling factor. Three cases are plotted in figure 2.3.2.

The most left plot has a low built-in strain, meaning the applied gate voltage pulls the membrane down and increases the tension in the drum. This increases the resonance frequency. The most right plot already has a high built-in strain, so the gate voltage has an electrostatic spring softening effect, decreasing the spring constant of the drum and thus lowering the resonance frequency. The middle plot is simply a combination of these two cases, where for low voltages, the built-in strain is larger than the extra tension due to the pulling of the membrane by the gate voltage, so spring softening occurs. At certain voltages, the extra tensions due to the static deformation of the drum by the DC gate voltage becomes the dominant tension, at which point the resonance frequency starts to increase again.

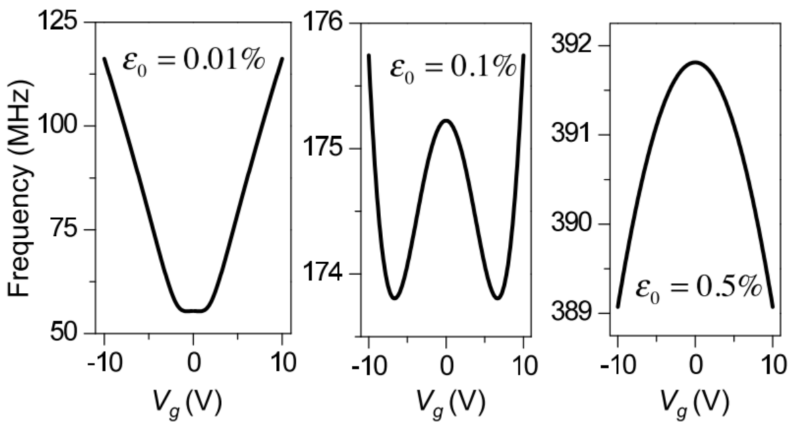

Figure 2.3.2: Behaviour of the resonance frequency as a function of the applied gate voltage. The value of the built-in strain free parameter ε_0 can result in three different types of graphes. From Chen [12].

Although this model should very nicely describe the measurements done during this thesis, the assumption that the membrane is thin enough to neglect its bending rigidity might not be valid for the slightly thicker membranes fabricated during this thesis. Therefore, an addition bending rigidity term might be necessary to fit the model with the measurement data.

2.4. INTERFEROMETER THEORY

The most important readout method of the resonance frequency of devices in this thesis is done with the interferometer setup. Two types of interferometry are commonly used, Michelson-Morley interferometry and Fabry-Perot interferometry. The first uses a single beam of light split into two beams where one beam is incident on the sample and the other onto a reference mirror. The beams then recombine and an interference pattern results [6]. However, during the course of this thesis, a Fabry-Perot interferometer setup is used, so the emphasis on this theoretical explanation will be on this type of interferometry.

In Fabry-Perot interferometry, a single beam of light is incident on a partially reflecting material, acting as the first mirror. Part of the beam is transmitted and is reflected on a back mirror which is (ideally) completely reflective. This second mirror is directly behind and parallel to the first mirror, causing the path of the beam reflected from the second mirror to overlap the reflected beam of the first mirror. The two reflected beams interfere and provide a detectable signal for a photodiode detector.

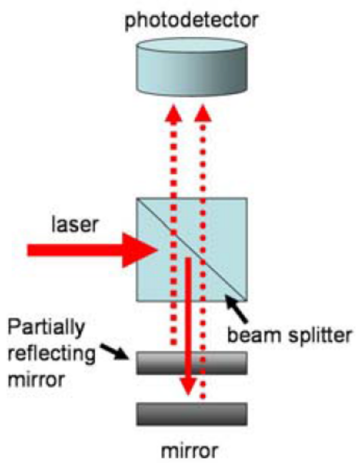

Figure 2.4.1: Schematic representation of a Fabry-Perot interferometer. The incident laser light is redirected onto the partially reflecting mirror and fully reflecting mirror. The photodetector acquires the interference signal from the two (dotted and dashed) lines. From Bunch [6].

A wide variety of 2D materials have the right characteristics to act as the first mirror. They are partially reflective, can be suspended parallel to a back mirror and due to a high thermal conductivity, they can be actuated with a laser modulated by a RF-signal. The Fabry-Perot interferometer detection method can be used in order to measure resonance frequency signals of because the first (partially reflecting) mirror is a moving suspended membrane. The motion of the drum causes a change in the interference pattern and therefore the quantity of light measured by the photodetector. This change in the measured signal by the photodetector equals the frequency with which the drum resonates, thus measuring the response of the system at certain frequencies.

In order to mathematically describe the light interaction, an analysis of all reflectivities and transmissions of the electric field caused by the laser light is required. When assuming the drum is a single layer and the phase difference that occurs within the drum is negligible, only the optical path difference between the drum and the back mirror determines the vibration dependent interfence, given by equation 2.27.

$$\delta = \frac{2\pi n d}{\lambda} \tag{2.27}$$

Where n is the refractive index of the material between the drum and the back mirror, so $n = n_{vacuum}$, d is the distance between the drum and the back mirror and λ is the wavelength of the laser light.

3

METHOD AND EXPERIMENTAL SETUP

To investigate the frequency of mechanical resonators, structures are made of suspended 2D materials. We start by discussing the fabrication of the substrates in section 3.1. Exfoliated membranes are then suspended over the patterned holes using a dry transfer method, described in detail in section 3.2. The measurements are done in an interferometer setup, explained in section 3.3. After initial measurements, modifications to the fabrication method and setup are made to facilitate the electrical actuation of membranes, explained in sections 3.1.2 and 3.4.

3.1. SAMPLE FABRICATION

The fabrication of the required samples is done in the Kavli Nanolab, positioned in the Van Leeuwenhoek Laboratory in Delft, which is a class 10000 clean room facility.

3.1.1. DEVICE GEOMETRY AND FABRICATION

To measure resonance frequencies and other properties of suspended membranes, two types of structures are commonly used: membranes suspended over circular holes (fully clamped drums) and membranes suspended over a trench (double clamped drums). These devices with well defined properties and are easy to model due to the possibility to treat them as one dimensional systems. At the start of this thesis, a test pattern was designed to accomodate several possible areas of investigation by creating a pattern with many different geometries. The following shapes are included in the pattern created with L-Edit software:

1. Circular holes of different diameters
2. Dumbbell shapes with varying diameters and varying distances between the two circular holes
3. Pillars in close proximity to one another
4. Squares with different side lengths
5. Trenches with different aspect ratios and lengths
6. Optical markers to navigate on the sample

Figure 3.1.1 shows examples of the different patterns as visible in the design software. The main pattern is divided into 64 smaller areas containing one of the patterns described above. The majority contains arrays of circular holes, since these are the most common structure to suspend membranes.

To create this pattern a standard electron beam lithography technique was used. A single side polished wafer is diced into 19 mm by 19 mm samples, with highly doped p-type silicon and a layer of thermally grown oxide layer (SiO_2) of 285nm thick. The fabrication steps from start to finish are:

1. Clean sample in nitric acid (HNO_3), sonicated for 5 minutes
2. Evaporation of chromium (Cr) on sample, thickness 30 nm
3. Cleaning in acetone for 30 seconds and isopropanol (IPA) for 30 seconds
4. Spincoating of 3% Anisole 950k PMMA (positive resist) at 3000 rpm (PMMA thickness 150nm)
5. Baking of PMMA for 20 minutes at 175°C
6. Writing the designed pattern with the EBPG
7. Developing the exposed PMMA in MIBK:IPA 1:3 for 90 seconds

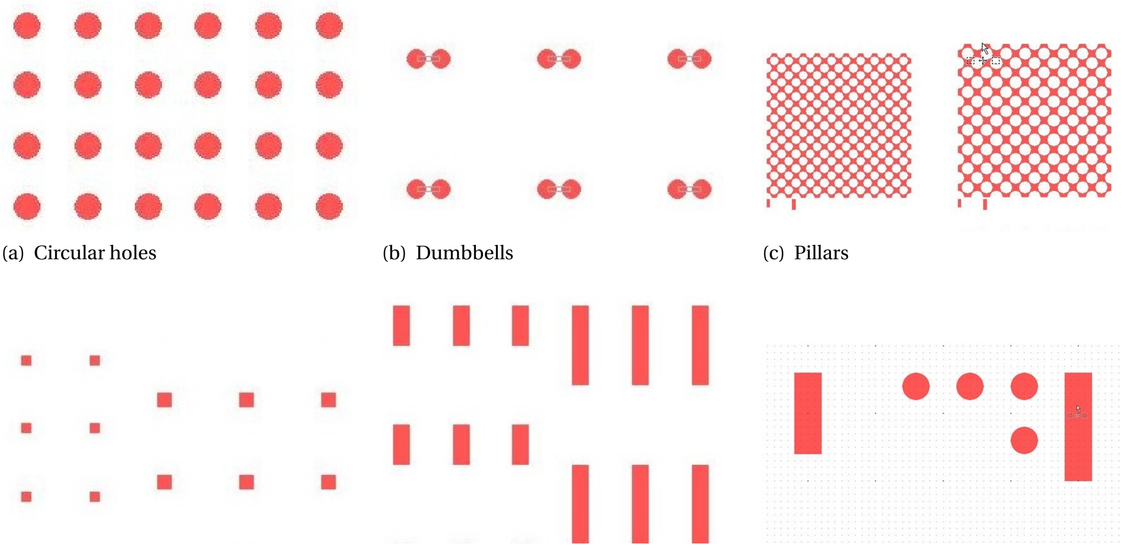

(a) Circular holes (b) Dumbbells (c) Pillars

(d) Squares (e) Trenches (f) Optical markers

Figure 3.1.1: Design pattern. Each pattern (except the markers) is repeated several times in a small array. Different arrays have different dimensions

8. Stop development of PMMA in IPA for 90 seconds
9. Etch the chromium layer with Chromium etchant CR-10 for 30 seconds, rinse with water
10. Strip remaining PMMA in hot ($50°C$) acetone bath
11. Reactive Ion Etching of silicon oxide using 50 SCCM CHF_3 and 2 SCCM Ar, low pressure ($7\mu bar$), $50W$, 20 minutes
12. Strip remaining Cr with CR-10
13. Spin protective resist S1813 at 2000 rpm
14. Baking S1813 for 5 minutes at $140°C$
15. Dice 19 mm by 19 mm samples into 16 smaller samples
16. Clean small samples in hot ($50°C$) acetone bath

The most important of the fabrication steps are illustrated schematically in figure 3.1.2.

After these fabrication steps, the finished samples have a silicon base with silicon oxide top layer of $285nm$, which includes the pattern. The silicon oxide is removed where the pattern was written by the EBPG. An example of how part of the substrate looks can be seen in figure 3.1.3, it shows 4 different sizes of hole, which are parts of 4 squares of one main pattern with 64 of those squares, which is defined as one sample. This entire pattern is written multiple times (preferably 16 times) when using the EBPG to use the time reserved on that device as effecient as possible. This means 16 identical samples are obtained in one fabrication batch.

3.1.2. FURTHER SAMPLE FABRICATION METHOD

In order to electrically actuate drums, two electrodes with an insulating layer in between are needed, a top electrode and a back gate. Conveniently, samples are fabricated on highly doped silicon wafers with a thermally grown silicon oxide layer on top. These act as the back gate and insulator respectively. Initial sample fabrication therefore consisted of the process described in section 3.1.1 without preforming step 12, so the chromium remains on the sample as top contact.

As became clear after the first set of experiments on the sample fabricated as described above in section 3.1.1, with the minor adjustments made to the existing interferometer setup described later in section 3.4, some alterations to the devices were necessary. First of all, a decrease in parasitic capacitance was needed in order to increase the effect of the electrical signal on the membrane. Initial samples had parasitic capacitances in the order of several picofarads, while this improved sample fabrication resulted in parasitic capacitances under 10 femtofarad. Secondly, a different metal needed to be used in order to prevent a capacitance between the metal layer and the 2D materials, because the chromium sample slightly oxidized, forming an insulating layer between the metal and membrane. Thirdly, an increase in capacitive coupling between the

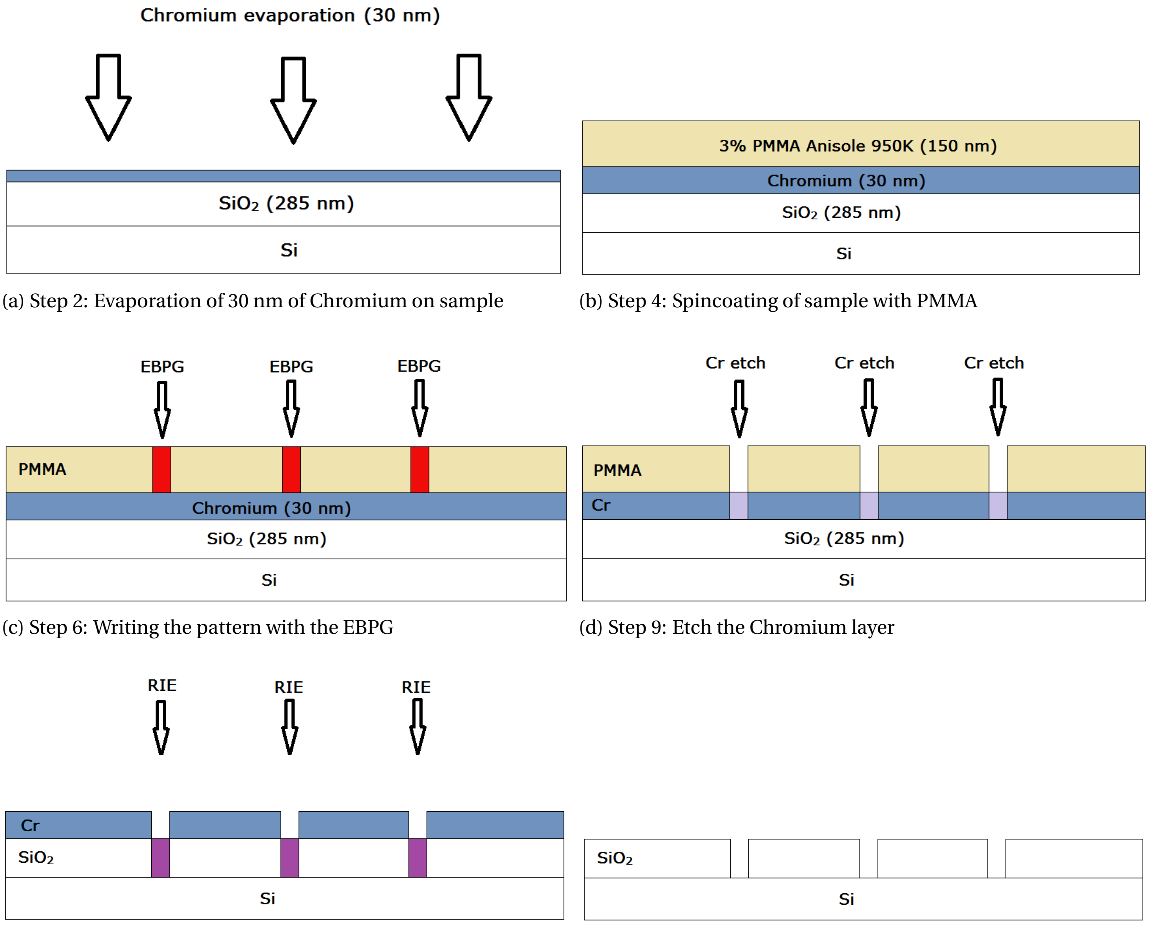

(a) Step 2: Evaporation of 30 nm of Chromium on sample

(b) Step 4: Spincoating of sample with PMMA

(c) Step 6: Writing the pattern with the EBPG

(d) Step 9: Etch the Chromium layer

(e) Step 11: RIE of silicon dioxide

(f) Step 12: Etch the remaining Chromium

Figure 3.1.2: Schematics of the most important steps in the fabrication proces.

membrane and back gate would improve the range of frequency tunability with lower gate voltages. The changes in fabrication method to achieve these improvements are explained in the following sections.

3.1.3. DECREASE IN PARASITIC CAPACITANCE

To decrease the parasitic capacitance, the pattern was redesigned. Figure 3.1.4 shows the new pattern.

Holes were used the most in the initial samples and therefore only holes of 2, 3, 4 and 5 μm in diameter were included in the new pattern. 16 holes of each diameter were positioned on a 140 μm by 140 μm sqaure, which is connected to a 200 μm by 200 μm bond pad. The area covered by conductive material is decreased from $20mm^2$ to $0,0596mm^2$, and since the parasitic capacitance is directly proprtional to surface area covered by metal, the parasitic capacitance will decrease from values in picofarads to femtofarads, which is calculated with the geometries of the different samples and equation 3.1.

$$C_p = \frac{\varepsilon_0 \varepsilon_r A}{z} \tag{3.1}$$

Where C_p is the parasitic capacitance, ε_0 is the permitivity of vacuum, ε_r the permitivitty of the insulator between the two layers, or the relative permitivitty. A represents the contact area and z is the distance between the two layers forming the capacitor.

To only have to expose the smallest area of the pattern, which are the bond pads and squares with holes, a different fabrication method is chosen. The process is schematically depicted in figure 3.1.5.

The image shown in figure 3.1.5a corresponds to the sample made by steps 1-6 in the recipe shown below. A bilayer of electron sensitive resist is created, where the top layer has a higher molecular weight than the

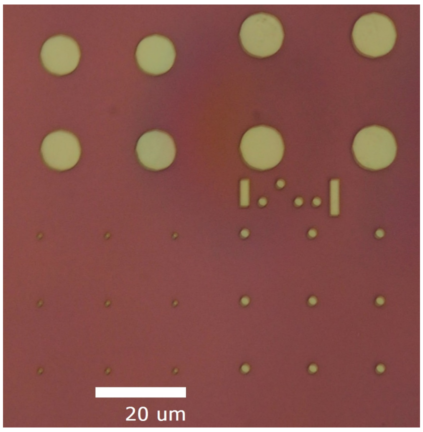

Figure 3.1.3: Several sizes of fabricated holes. The dark red part shows the silicon oxide, the lighter (yellow-green) circles show the places where the silicon dioxide was removed and a hole is formed (thus the silicons is visible). The holes on the bottom left have diameters of $1\mu m$, the holes on the bottom right have diameters of $2\mu m$, top left is $9\mu m$ and top right $10\mu m$. Optical markers are visible between the two rows of holes, which are used to navigate on the sample once it is loaded into the setup.

bottom layer (950k and 495k respectively). This means the electrons writing the pattern will scatter less in the top layer and more in the bottom layer. The reason for choosing this method is the undercut resist profile that is formed after exposure and development (figure 3.1.5b), which is advantageous for the lift-off process. The evaporation of metals should not result in a layer of metal on the sidewall of the PMMA, because that would make it increasingly difficult to remove the resist and metal on top of the resist. The undercut profile prevents deposition of a vertical layer over the entire height of the resist profile, as can be seen in figure 3.1.5c.

1. Clean sample in nitric acid (HNO_3), sonicated for 5 minutes
2. Cleaning in acetone for 30 seconds and isopropanol (IPA) for 30 seconds
3. Spincoating of 6% Anisole 495k PMMA (positive resist) at 4000 rpm (PMMA thickness 325nm)
4. Baking of PMMA for 20 minutes at $175°C$
5. Let sample cool for 5 minutes
6. Spincoating of 3% Anisole 950k PMMA (positive resist) at 4500 rpm (PMMA thickness 125nm)
7. Writing the designed pattern 9 times with the Electron Beam Patttern Generator (EBPG)
8. Developing the exposed PMMA in MIBK:IPA 1:3 for 90 seconds
9. Stop development of PMMA in IPA for 90 seconds
10. Evaporation of platinum (Pt), thickness 5 nm, gold palladium (Au/Pd), thickness 90 nm, chromium (Cr), thickness 30 nm
11. Lift-off PMMA layers and metal on top of those PMMA layers in hot ($50°C$ acetone bath, 1 hour
12. Reactive Ion Etching of silicon oxide using 50 SCCM CHF_3 and 2 SCCM Ar, low pressure ($7\mu bar$), $50W$, 20 minutes
13. Strip remaining Cr with CR-10
14. Spin protective resist S1813 at 2000 rpm
15. Baking S1813 for 5 minutes at $140°C$
16. Dice 19 mm by 19 mm samples into 9 smaller samples
17. Clean small samples in hot ($50°C$) acetone bath

Another change of the new fabrication method compared to the initial process explained in section 3.1.1 is the evaporation of metals. The choice is made to use gold palladium (Au/Pd) as a contact metal to stamp the membranes on and make the electrical connection (on the bond pads). Au/Pd is chosen for several reasons. It does not oxidize, so will not create any additional capacitance between the metal and the membranes. Also, Au/Pd has a high conductivity and is robust, which is important for wirebonding. Finally, it can be evaporated in amorphous layers, which is important to form a smooth surface to stamp on. The only disadvantage of Au/Pd is that its lattice constant does not match that of silicon oxide (SiO_2) very well, which is why a $5nm$ layer of titanium (Ti) is evaporated first. Ti matches the lattice constants of both SiO_2 and Au/Pd reasonably well, making it a suitable connecting layer. The evaporation of the three layers is visualized in figure 3.1.5c and the final product without chromium (after step 13 in the recipe) can be seen in figure 3.1.5f.

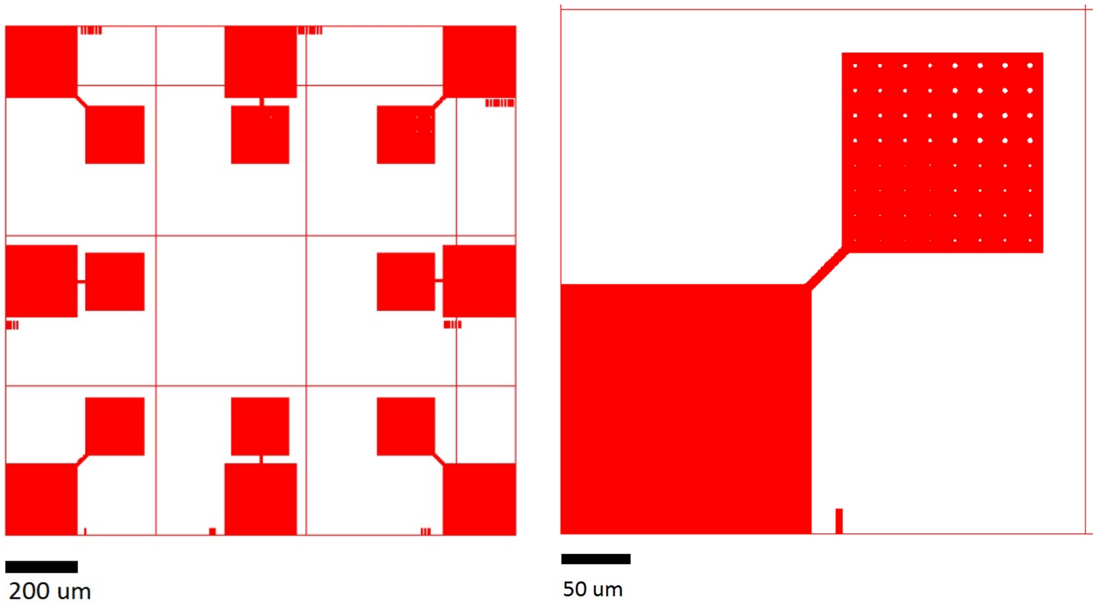

(a) Overview

(b) Zoomed in view of one pattern

Figure 3.1.4: The new design consist of 9 patterns. Each pattern includes holes of 2, 3, 4 and 5 μm in diameter on a 140 μm by 140 μm square, connected to a 200 μm by 200 μm bond pad.

3.1.4. INCREASED CAPACITIVE COUPLING

The last modification to the sample fabrication that was made was the use of different wafers. A wafer with equally p type doped silicon, but with a layer of thermally grown silicon dioxide that is less thick was used. The silicon oxide layer in the initial samples has a thickness of $285nm$, whereas the last batch of samples have a silicon oxide thickness of $50nm$. This is meant to increase the capacitance between the suspended membranes and the silicon back gate, since the capacitance of the membrane scales proportional to $1/h$, where h is the height of the cavity between the membrane and the back gate. Qualitatively this means that the capacitive coupling increases. The same voltage difference between the top metal layer (and thus the membrane) and the silicon back gate will translate to a bigger electrical force on the membrane and therefore a larger deflection. This equals a larger amplitude of motion generated by the same RF modulates, which results in an improved interference signal.

Another advantage of the increased capacitive coupling is the increased sensitivity in the deflection from the equilibrium position of the membrane as a result of a DC voltage over the top gate and back gate. The gate tuning explained in section 2.3 will be possible to a greater extend with lower applied voltages.

(a) Spin resist on sample

(b) Writing pattern with EBPG + develop

(c) Evaporate metal layers

(d) Lift-off resist layers and metal on those layers

(e) RIE of silicon dioxide

(f) Chromium etch

Figure 3.1.5: A standard lift-off procedure is used to fabricate the new samples. A detailed list of all fabrication steps can be found below.

3.2. STAMPING TRANSFER METHOD OF 2D MATERIALS

The stamping transfer method originates from the scotch tape exfoliation technique used in the discovery of graphene by Novoselov *et al.* [3]. In this thesis, elastic blue tape is attached to bulk crystals and ripped off to mechanically exfoliate single layers of material, hence two dimensional materials. Geim and Novoselov have started a new field of experimental methods to obtain not only graphene, but many other two dimensional materials [4]. One of those methods is an adaption to the scotch tape method, developed by Andres Castellanos-Gomez. It is an all dry exfoliation and transfer method developed to specifically position two dimensional materials at certain locations and is very well explained in the supplementary information from Castellanos-Gomez *et al.* [34]. Figure 3.2.1 shows a schematic description of the procedure.

After the flakes of the desired two dimensional material are exfoliated and transferred to the viscoelastic stamp (the polymer in figure 3.2.1), flakes with a certain upper limit of thickness have to be located in order to preform consistent measurements on different flakes. The amount of layers can be estimated when investigating the viscoelastic stamp under an optical microscope and using the transmission mode. Figure 3.2.2 indicates the difference between several amounts of layers of material. However, these will remain estimates, a conclusive measurement is done by AFM to obtain the actual thickness of each flake after it has been stamped on a sample.

Knowing the position of each flake thickness, the desired number of layers of part of a flake can be positioned over a hole as shown in figure 3.2.1. The glass plate is inserted in a micrometer xyz-stage, giving complete freedom of where on the sample a flake will be transferred.

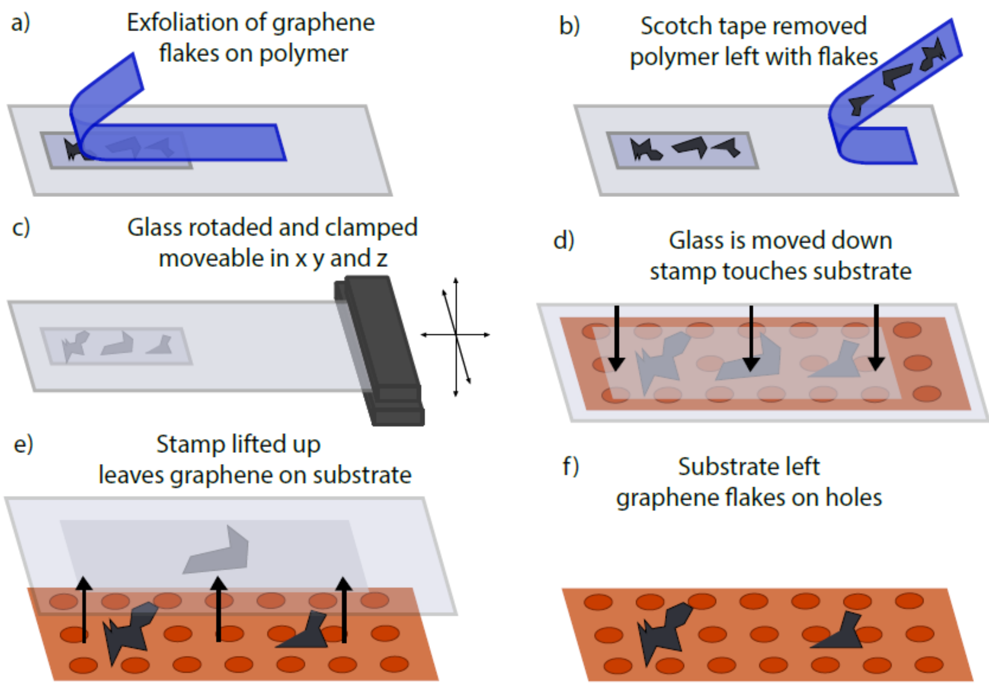

Figure 3.2.1: The all dry exfoliation and stamping method developed by Castellanos-Gomez *et al.* [34] depicted in six steps. The flake size is enlarged greatly for explanation purposes, a microscope is needed to locate the actual flakes, with sizes in the order of tens of micrometers. Taken from de Koning [35].

3.3. LASER INTERFEROMETER SETUP

During the course of this thesis, the laser interferometer setup is used to preform resonance measurements. The setup uses two different laser sources, one laser actuates the drum and a second laser to probe that motion of the drum. First, the existing setup and measurement equipment is explained, to create an understanding of the current possibilities of measurements. Modifications to the setup to enable electrical actuation of membranes as explained in section 3.4 are made.

A laser interferometer is based on the principle that a difference in optical path length between two beams causes an interference pattern. The theory of the physics behind this principle is explained in section 2.4. A schematic overview of the setup can be seen in figure 3.3.1.

The setup is explained by following the path of the red laser and explaining each component. Naturally, the first part is the Helium-Neon laser of $\lambda = 633nm$, which generates the laser light that probes the motion of the graphene drum. A variable neutral density filter is used to control the intensity of the laser light. The maximum output of the laser is $24.1mW$, while the intensity is typically attenuated by the neutral density filter to values around $10mW$ to reduce excessive heating of the membranes. After losses caused by slight scattering of the laser light due to imperfections in the mirrors and lenses, a laser power of several milliwatts is used to probe the membrane.

The next component is a beam expander and spatial filter, consisting of a combination of two lenses with different focal distances to increase the beam diameter. The first lens has a focal distance of 50mm and the second lens has a focal distance of 150mm. A pinhole is placed exactly in the focal point of both these lenses to filter any scattered light. The pinhole acts as a spatial filter and together with the second lens provides plane waves with a gaussian intensity profile for the rest of the optical path. The beam expander/spatial filter combination is designed to completely backfill the objective lens (present right before the vacuum chamber). This increases the efficiency of the setup by using all the laser power of the beam entering the objective lens to probe the motion of the graphene drum.

After the beam expander, the incoming Helium-Neon laser light travels through a polarizing beam splitter

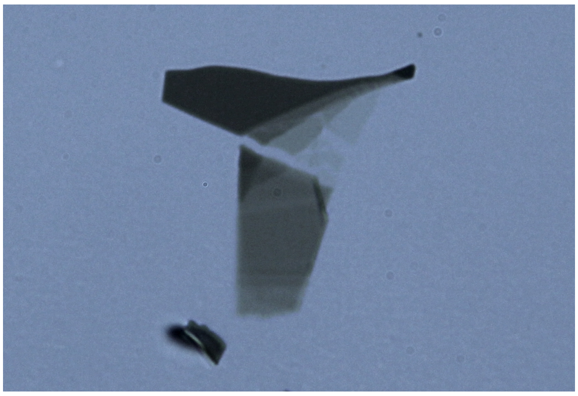

(a) Transmission micrscope image of flakes

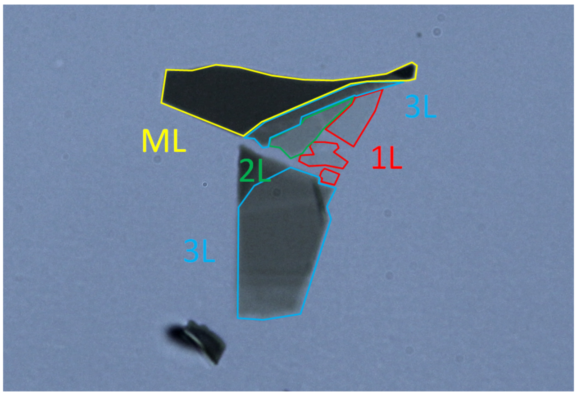

(b) The same image with layer thickness indication

Figure 3.2.2: An example of a transmission microscope image taken of a flake of MoS_2 both with and without indication of the number of layers. The intensity of the flake against the background gives a rough estimate of the layer thickness when the flake consists of several layers of materials, but with single layers it can more easily be distinguished. 1L: monolayer, 2L: bilayer, 3L: trilayer, ML: multilayer

and quarter wave plate. Together with the quarter wave plate, the polarizing beam splitter affects the beam returning from the vacuum chamber. This part of the setup provides a menas of seperating the incoming light from the returning light before it reaches the photodiode (PD). The incoming beam is linearly polarized when it reaches the polarized beam splitter, but becomes cicrularly polarized when passing the quarter wave plate. The phase of the Helium-Neon laser light changes 45° upon each passing, so the return beam has a 90° phase difference from the incoming beam at the polarizing beam splitter. This splitter transmits the linearly polarized light coming from the laser, but reflects the circularly polarized light returning from the sample. After the light is reflected it is focussed on the photodiode by another lens with a focal distance of 40mm. The photodiode detector acquires the signal returning from the sample in the vacuum chamber, which quantifies the variation in intesity due to the motion of the drum. It operates in the MHz range, the detector used during the course of this thesis is able to measure frequencies from DC-125 MHz.

The sample in the vacuum chamber can be positioned exactly to align the laser light with the resonator. The membranes that are measured have diameters in the order of micrometers, which is impossible to see with the naked eye. To position the laser light precisely on the membrane of interest, a white light source (LS) in combination with the CCD camera is used to image the surface of the samples inside the vacuum chamber. The laser beams are temporarily blocked and the vacuum chamber, mounted on a stage with micrometer screws, is positioned so that the membrane is in focus and at the right position in the focal plane. This is possible because the CCD is placed at a 90 degree angle from the surface of the sample to prevent it from blocking the laser beams. However, the beam splitter used for this (M: 50% mirror) not only reflects 50% of the white light used to image the surface of the sample, but when measuring, it also reflects 50% of the laser light, causing a loss of 75% in laser power (because half of the light is lost in both the incoming and return beams). This is undesirable, so the beam splitter is placed on a flip mount instead of a fixed mount to allow it to be removed from the optical path once the position of the membrane is aligned with the optical path of the laser.

As mentioned before, the last component before the vacuum chamber is the objective lens. It provides a magnification of 50 times and is placed in close proximity to the next component, the vacuum chamber.

Samples are placed inside a small vacuum chamber so that measurements can be done at vacuum, which has two reasons. Firstly, the membrane should not interact with gas molecules in the air, because this causes differences in resonance frequencies. When gas molecules adhere to the surface of the drum, the effective mass is changed, changing the resonance frequency. This effect can be quite significant and affect the frequency tuning experiment in this thesis. Secondly, a movement of the membrane induces a pressure difference between the cavity and the surrounding environment, which counteracts the actuation of the membrane by the blue diodelaser. Graphene (and other 2D materials) are impermeable when in perfect condition. In case gas molecules are trapped in the cavity (between the drum and the substrate), the space they are confined in becomes smaller once the drum is deflected towards the cavity, thus increasing the pressure inside the cavity. This leads to a net force outwards, decreasing the effect the actuation has on the actual deflection. The same goes for the deflection of the drum away from the substrate, the volume increases, pressure

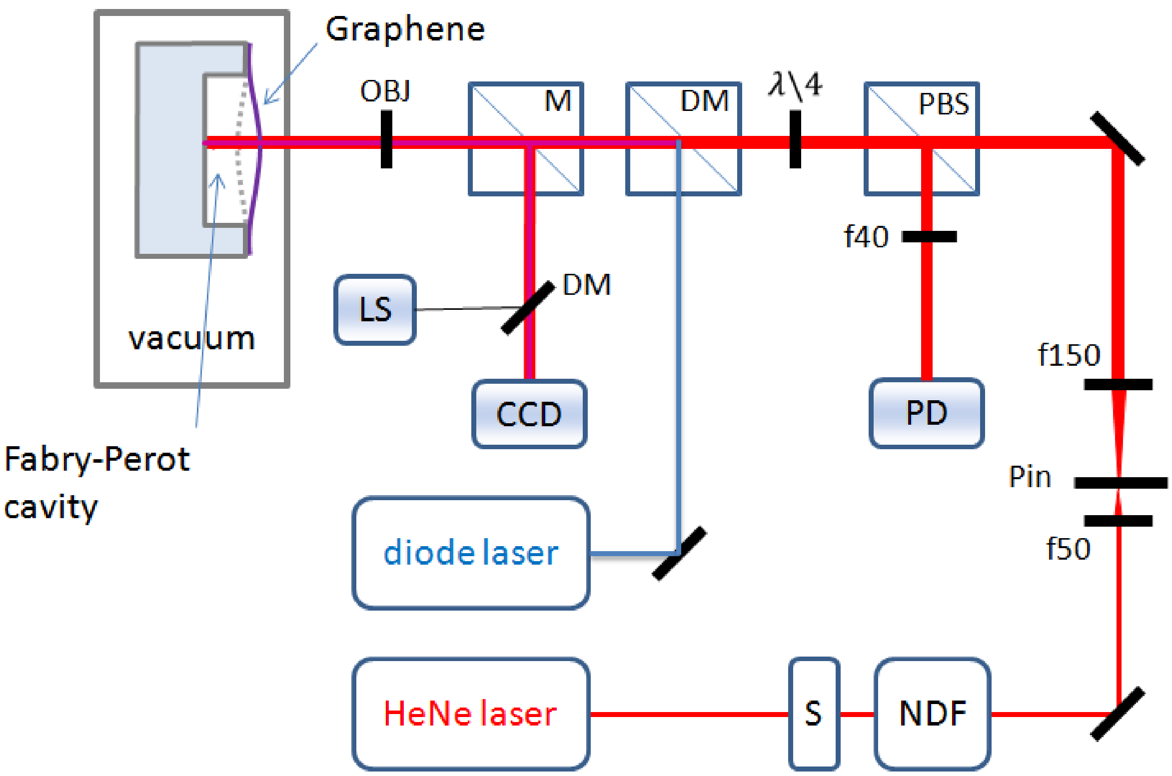

Figure 3.3.1: Laser interferometer schematic. S: shutter; NDF: neutral density filter, Pin: Pinhole, PBS: polarizing beam splitter, PD: photodiode, M: 50% mirror, DM: dichroïc mirror, CCD: imaging camera, OBJ: 50x objective lens, LS: light source.

decreases and the actuation is counteracted.

The entire vacuum chamber is placed on a micrometer xyz-stage, so it is possible to locate the resonator in the vacuum chamber and focus the laser spot on the correct part of the sample. The vacuum chamber and xyz-stage can be seen in figure 3.3.2.

The Fabry-Pérot cavity in the vacuum chamber, responsible for the interference of the Helium-Neon laser, exists between two mirrors; the front mirror being the graphene membrane and the back mirror being the silicon surface of the sample. Due to the motion of the membrane, the optical path length of the Helium-Neon laser changes and the interference between the two reflected laser beams changes in amplitude, with a frequency equivalent to the resonant motion of the drum. This is the signal detected by the photodiode.

The graphene membrane is excited by a $\lambda = 405nm$ (blue) diode laser, the last part of the setup to be discussed. The output power of the blue laser is modulated by a radio frequency (RF) signal. In most cases the drum is driven at its fundamental mode, but higher order modes can also be driven. Due to the geometry of the sample, in-plane motion is not really present and out-of-plane motion is dominant. The blue diode laser is aligned with the Helium-Neon laser, to make sure the actuation and probing of the membrane occur at exactly the same position. This alignment is done with the dichroïc mirror. This mirror either transmits or reflects light depending on the wavelength of the light. This way, the blue laser light is reflected, while the red light is transmitted. Both the alignment of the incoming beams and the separation of the return signal are done by this mirror. Due to the reflection at the dichroïc mirror, the blue laser light reflected by the sample does not reach the detector and the measured signal only consist of the interference of the Helium-Neon laser.

As can be seen in figure 3.3.3, the entire setup is mounted on an optical table with active vibration isolation to prevent any vibrational noise to occur in the measurements.

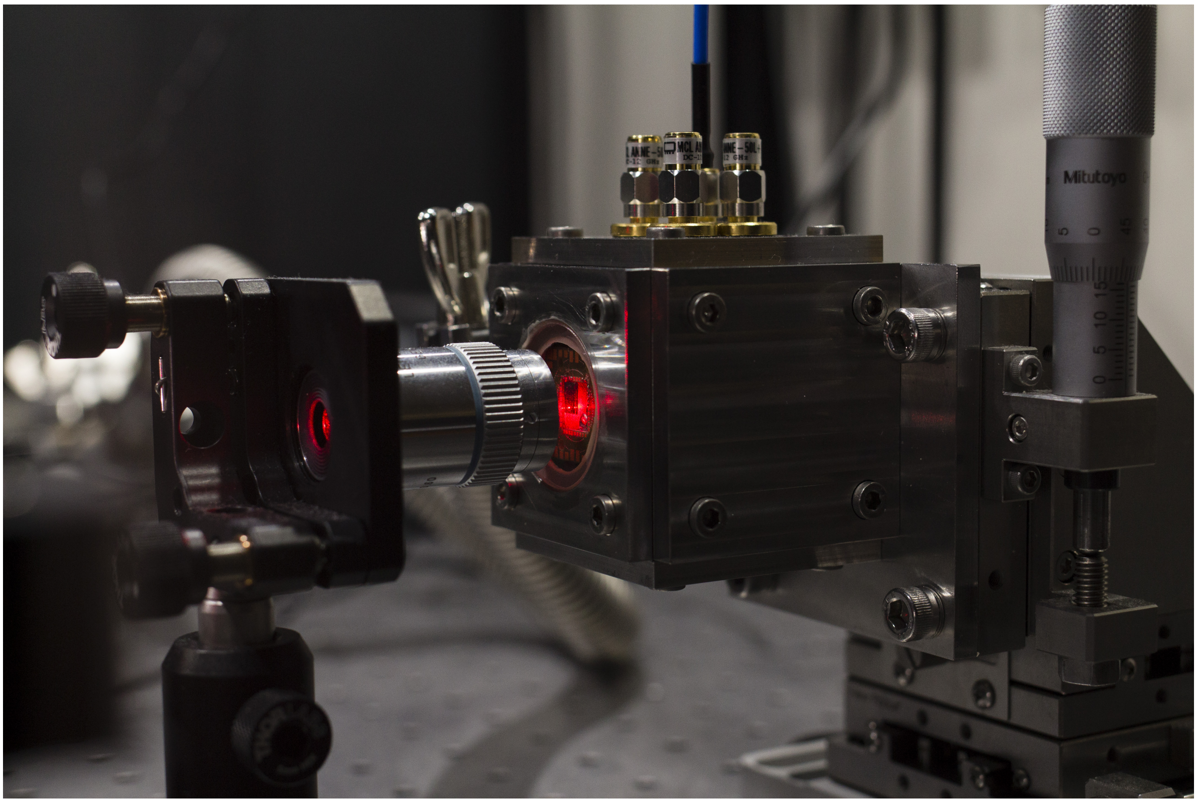

Figure 3.3.2: A photograph of the vacuum chamber secured on a xyz-stage. On the left, the objective lens is visible, focussing the red Helium-Neon laser light on the sample in the vacuum chamber. On top of the vacuum chamber are three 50Ω terminators and one SMA cable. The right side of the picture shows one of three micrometer screws which controls the position of the vacuum chamber.

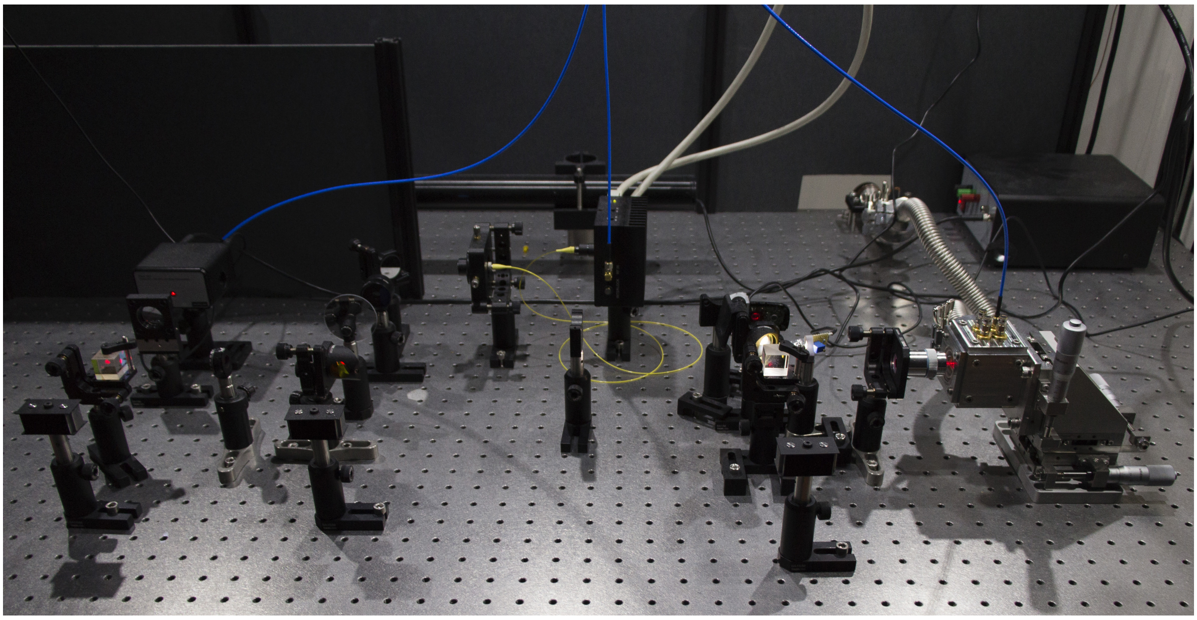

Figure 3.3.3: A photographs showing the optical table with all the equipment secured at exact positions to ensure the best alignment possible.

3.4. ELECTRICAL ACTUATION SETUP

To enable electrical actuation, slight modifications to both the fabrication method and interferometer setup are made. The following section explains the very basics that are needed to test the possibility of electrical actuation of membranes in the current setup. Also, a short description of some of the setup equipment is given and further improvements to both the samples and setup are discussed.

Electrical actuation of mechanical resonators does not require many modifications to the intereferometer setup either. Naturally, the thermal actuation done by the blue diode laser, is replaced, so the laser light is blocked. Additions to the setup can be seen in figure 3.4.1.

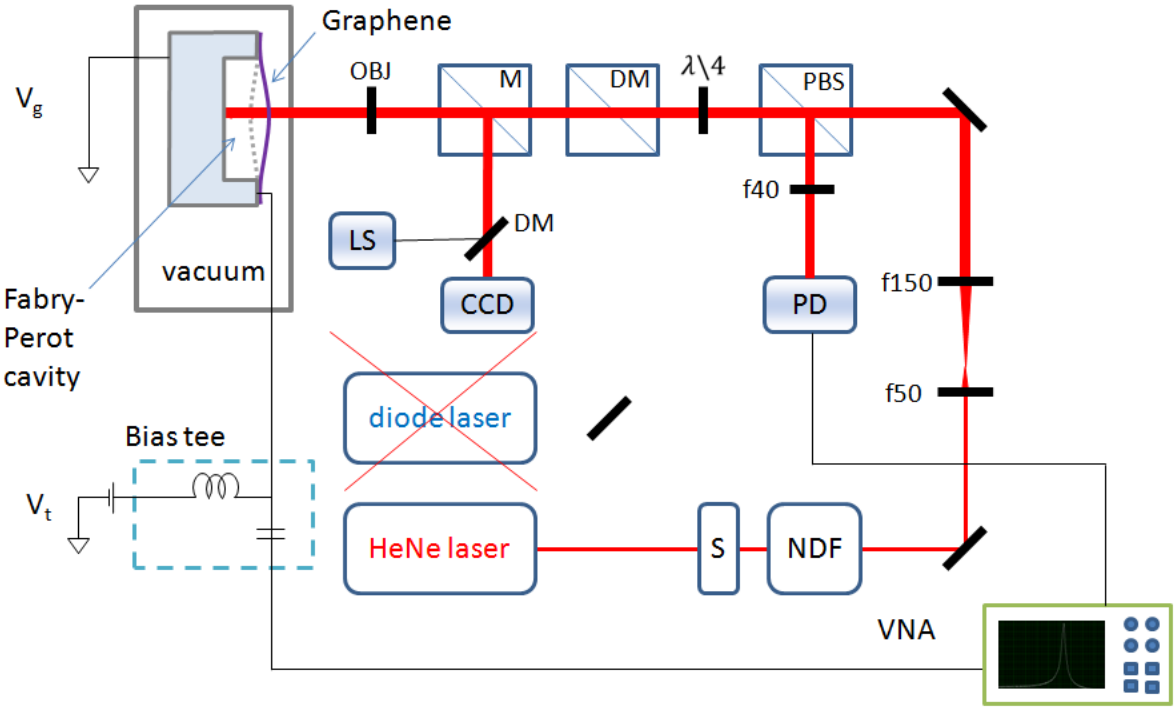

Figure 3.4.1: Laser interferometer plus electrical actuation schematic. All components are the same as in figure 3.3.1, expect the following: V_g: grounded back gate; V_t: top layer voltage; VNA: Vector Network Analyzer. The graphene membrane is actuated by a potential difference between the top layer and back gate of the sample instead of the thermal actuation by the blue laser. The red laser still probes the membrane motion.

The electrical signal is a combination of a sine wave at radio frequencies and a DC signal used for frequency tuning of the resonator. These two signals are combined in a bias tee, of which the output is the signal connected to the vacuum chamber. As explained below, the VNA, here depicted as component 13, has an output RF signal which is connected to the bias tee and the input signal is fed back into the VNA from the photodiode.

Some modifications to the vacuum chamber are made. Samples are secured on chip carriers and can be electrically connected through SMA connectors in one of the vacuum chamber plates. The SMA connectors can be seen in figure 3.4.2. The back gate of the sample is also connected to one of the SMA connectors and terminated with a 50 Ω resistor to serve as ground.

Two important pieces of measurement equipment in the setup are the Vector Network Analyzer and the Spectrum Analyzer.

The Vector Network Analyzer (VNA) is the main piece of measurement equipment used in this thesis. It provides a modulated RF signal as the source of actuation (either via the blue diode laser or directly to the top gate of the sample). A certain desired frequency range can be set to investigate, so the VNA sends out a signal at several data points within the set frequency range (a typical number of data points is 1001). The AC-component of the signal measured by the photodiode detector is then fed back to the VNA and compared as an input value to the output value at each data point. This method provides the normalized transfer of the setup in V/V, which is used for further data analysis in MATLAB.

The Spectrum Analyzer (SA) can be used to measure the thermal motion of a membrane. For certain measurements, no actuation is required and the membrane will resonate as a result of the thermal energy present in the system. All measurements in this thesis are done at room temperature ($295K$), meaning $E_{th} = k_B * T$. For thin membranes, this is enough energy to trigger a resonance.

The photodiode (PD) measures the interference signal of the Helium-Neon laser. It seperately provides the DC and RF components of the detected signal, with the RF signal fed back into the VNA for the S_{21} measurement. It can measure signals in a frequency range of DC-125MHz.

The voltage source provides a DC voltage that deflect the suspended membrane and therefore controls the frequency tuning. Both the voltage source and VNA can be controlled by a pc so measurement parameters can be altered easily and measurement data can be stored quickly and efficiently.

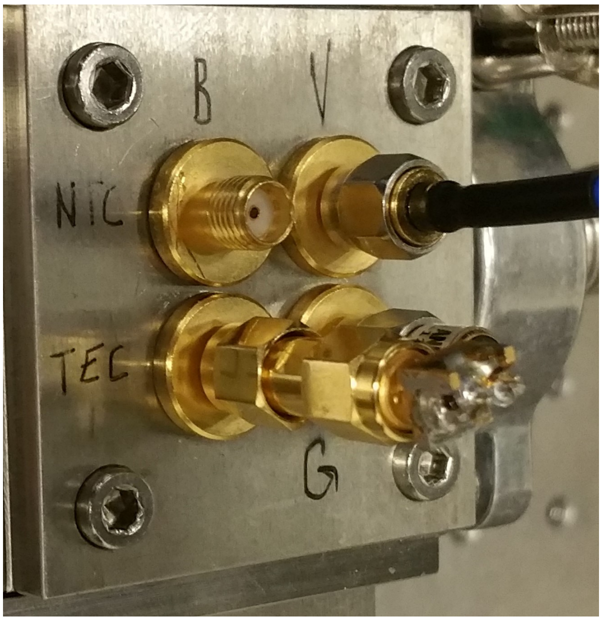

Figure 3.4.2: The SMA connectors that provide an electrical connection from the outside of the vacuum chamber to the inside of the vacuum chamber.

4

RESULTS AND DISCUSSION

Results of the experiments performed during this thesis are reported and discussed in this chapter. Section 4.1 described the inital tests investigating the possibilities and performance of electrical drive integrated in the interferometer setup. In the next section (4.2.1) results of samples made with an improved sample fabrication are compared to the results of the same measurements done with the initial samples. Afterwards, in section 4.3, results of the frequency tunability of these improved samples is shown and compared to the model described in section 2.3.

4.1. ELECTRICAL DRIVE OF INITIAL SAMPLES

Initial samples consist of a silicon back gate substrate with a 285nm thick insulating silicon dioxide layer and a 30 nm chromium top gate as shown in section 3.1. Several flakes of graphene and molybdenum disulfide (MoS_2) were stamped on these samples to create resonators. The sample first investigated consisted of the described substrate and a graphene flake stamped on the chromium surface. The flake covered an area where the substrate holes have a diameter of 4 μm and is large enough to cover four holes, creating four circular suspended membranes. An optical image of the sample can be seen in figure 4.1.1.

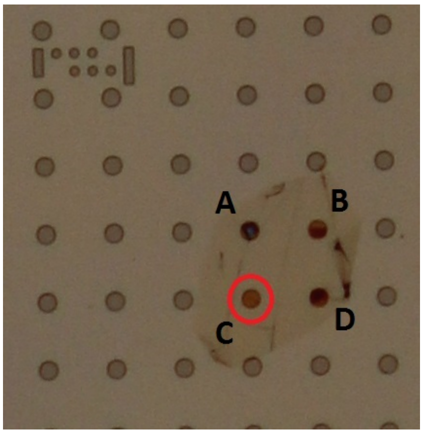

Figure 4.1.1: An optical image of the sample on which the first electrical drive measurements were done. A graphene flake is stamped on holes of 4 μm diameter. The flake is 7nm thick (measured with an AFM). Four drums are made, although there are some wrinkles in the flake. Measurements are performed on the drum encircled in red (drum C).

The creation of the four drums om a single flake gives the possibility to measure resonance frequencies of similar drums due to the same initial conditions (pre-tension mostly) and dimensions. However, there are some wrinkles in the graphene flake, covering two of the four holes (drum A and D). Drum B appears to be buckled when observed in the AFM measurement that was also used to determine the thickness of the graphene flake. Both buckled membranes and drums with wrinkles across their surface have resonance frequencies that are affected by these phenomena, leaving the hole encircled in red to perform the electrical acutation measurements.

4.1.1. POSSIBILITY OF ELECTRICAL DRIVE

The initial test of electrical drive integrated in the interferometer setup was done by applying the modulated RF signal on the top gate while having the back gate grounded. Initial measurements show a resonance peak at similar resonance frequencies and comparable Q-factors as the reference measurements done with the optical actuation, such as figure 4.1.3.

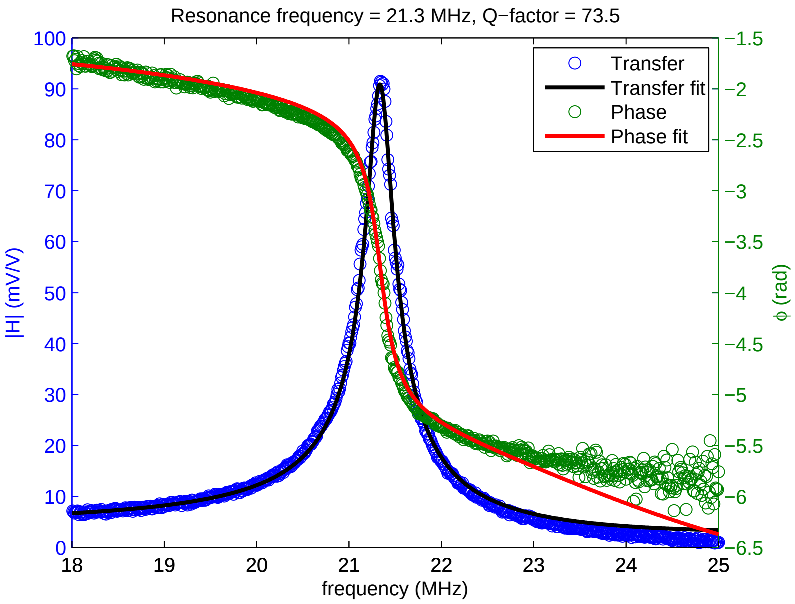

Figure 4.1.2: Optical actuation

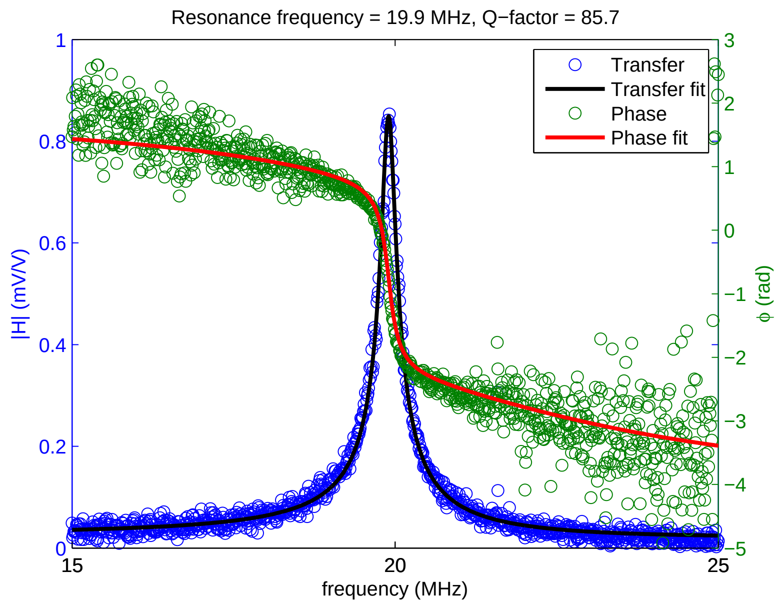

Figure 4.1.3: Electrical actuation

Figure 4.1.2 shows the magnitude and phase data together with its fitted plots for the optical actuation.

The laser that provides the optical actuation is set at - 25 dBm, at 7 mW. Figure 4.1.3 shows the same graphs, but the drum is actuated electrically, with a driving power of 0 dBm. Note the differences in magnitude amplitude, the optical signal gives a much higher peak. The phase data has different offsets, but both graphs show a phase change of π at the resonance frequency.

It is expected that the resonance frequency of both driving methods is the same, since we still drive with powers such that the drum resonates in the linear regime. There are slight differences, due to the heating of the membrane by the laser that occurs when actuating optically. This is explained in detail by Adiga *et al.* [36] and is one of the reasons for the addition of electrical actuation in the current interferometer setup. Figure 4.1.3 shows that the resonance frequency is similar (but not equal) for the two actuation methods. The fitted resonance frequencies and Q-factors are added as a title figures 4.1.2 and 4.1.3.

Several more observations can be made from these initial measurements. The amplitude of the magnitude signal is significantly higher for optical actuation, since the samples and setup for these initial measurements are optimized for optical actuation and not for electrical actuation. It is with the initial samples not known what the optimal device properties and setup settings are. The noise of the data collected when driving the drum electrically is substantially higher than that of the optically driven drum when using the sample amplification settings on the setup. This possibly indicates that the resonance amplitude is also lower for the electrical drive. A larger influence of the noise means that the signal is smaller in amplitude for the electrical drive compared to the optical drive, because the measured signal is divided by the input signal, meaning a smaller signal will show more fluctuations. It can be concluded that the optical drive provides a better coupling between the drive signal and the resonance amplitude. The provided driving power results in a certain resonance amplitude and the while this remains in the linear regime, the driving power can be increased to provide a larger force on the membrane and cause it to resonate more. However, it appears that in the case of the electrical drive, an increase in power that is put into the system does not result in a higher resonance amplitude as effectively as when the drum is driven optically. The measurements explained in the following sections, where a DC voltage is applied to deflect the membrane with a certain offset, provide a better and more complete understanding of why the coupling is not very good for this sample.

To conclude, electrical actuation is certainly possible in the initial measurements. The resonance frequency and Q-factor are comparable, the Q-factor of 85.7 for electrical actuation is already slightly higher than the 73.5 obtained during optical actuation. However, electrical actuation has a much smaller amplitude and is therefore more influenced by noise in this sample.

4.1.2. FREQUENCY TUNING WITH DC VOLTAGE

Another test that could be done with the initial samples was to check the possibility for frequency tuning with a DC voltage applied to the top gate by deflecting the suspended membrane as explained in section 2.3. This experiment was also done with the first sample in order to test if any changes needed to be made to the setup or sample fabrication method.

The drum is actuated electrically and the DC voltage is increased from 0 V to 7 V in steps of 0.1 V. After each step of 0.1 V, the response of the drum is measured, providing the same data as described in the previous section.

Upon investigation of the data presented in figure 4.1.4, several qualitative conclusions can be drawn. First of all, the resonance frequency appears to decrease as a result of the increasing DC voltage. The voltage does not affect the resonance frequency of the drum from 0 V to approximately 4 V. However, after 4 V, the spring constant of the drum starts to decrease due to the electric field, showing the electrostatic spring softening discussed in section 2.3. The resonance frequency decreases from roughly 20 MHz at 4 V DC to 18.5 MHz at 7 V, which means the frequency is tuned with a sensitivity of 0.5 MHz/V. This is not in the same order of magnitude obtained in measurements by Chen *et al.* [12], which claim tuning sensitivities up to 8 MHz/V. However, with the improved device geometry described in section 3.1.2, these sensitivities might be realized in the inteferometer setup as well.

Secondly, the magnitude graph shows that as the DC voltage increases, the amplitude of the magnitude signal also increases. The colourscale clearly indicated a vast increase in amplitude, processing of the data shows the amplitude increases from less than 0.5 mV/V at a DC voltage of 0 V to over 2 mV/V. This is more clearly shown in figure 4.1.5. The increase in amplitude will be discussed in greater detail later, due to a limited range of experiments that can be done with the initial sample, as will become clear later.

Most important in this figure are the lower resonance frequency and the higher amplitude for higher DC voltages. As was observable in figure 4.1.4 is now confirmed when looking at the seperate traces of 0 V and

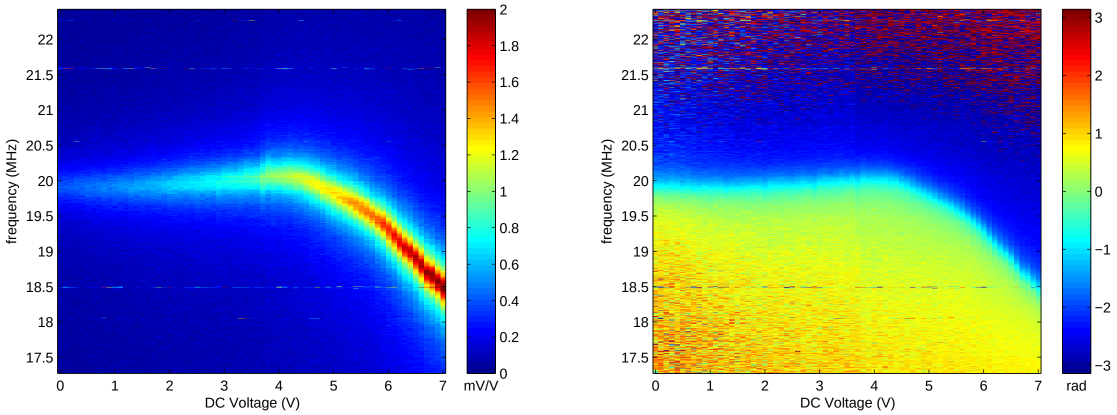

(a) (b)

Figure 4.1.4: The plots of both magnitude and phase data with DC tuning of the drum. As figure 4.1.4a shows, the resonance frequency can be observed to decrease for increasing DC voltages. Figure 4.1.4b shows the phase data, again showing a phase shift of π at the resonance frequency in correspondence with the magnitude data. The resonance frequency can clearly be observed to decrease from this figure as well, as the phase change shifts to decreasing frequencies for higher DC voltages.

7 V: the resonance frequency is decreased and the amplitude is increased for higher DC voltages when using electrical actuation. Explanations for these phenomena follow later, in section 4.3. There is another noteworthy point to be made about figure 4.1.5. The shape of the resonance peak remains symmetrical, meaning our nanomechanical resonator is still operating in the linear regime. This is very important to maintain to be able to process the obtained data further, as models to describe the nonlinear behaviour of resonators can become rather complex. Therefore, there will be no experiments performed during this thesis to investigate nonlinear effects.

Since electrostatic spring softening is the main cause of resonance frequency shifts, it is expected that the frequency decreases. When looking purely at the mechanical behavious of a sping, a softer spring resonates slower, thus with a lower frequency, and has a larger displacement. This is exactly what is seen in figure 4.1.5

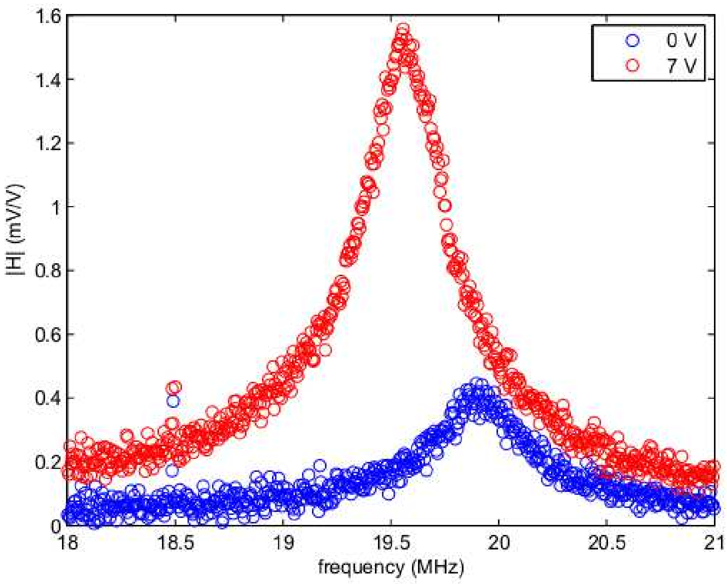

Figure 4.1.5: Traces of figure 4.1.4 taken at 0 V and 7 V. The increase in amplitude due to the DC voltage as shown here is apparent in all following measurements and will be discussed in further detail later in section 4.3.1. The shift in resonance frequency is also obvious in this plot.

Data processing is done using MATLAB. Each data trace containing information about how the resonance frequency depends on the DC voltage has to be fit to the model of the simple harmonic oscillator (SHO). This means each seperate trace, or frequency spectrum, has to be fit to the model. Therefore, each trace provides a specific resonance frequency, quality (Q) factor and amplitude, so this data can be plotted as a function of DC voltage. A modified program runs through the DC voltage spectra obtained at steps of 0.1 V, fitting each dataset, like the graphs in figure 4.1.5, to the simple harmonic oscillator model. This fitted data can then be used to reconstruct the 3D colourplot as shown in figure 4.1.4a. The model combines the magnitude and phase data to obtain a complex amplitude of the drum and provides several parameters, including amplitude, phase and resonance frequency. When plotting the resonance frequency parameter the model provides as a function of the DC voltage, a clear graph for this relation is obtained. This can be seen in figure 4.1.6, together with the reconstruction of the 3D colourplot.

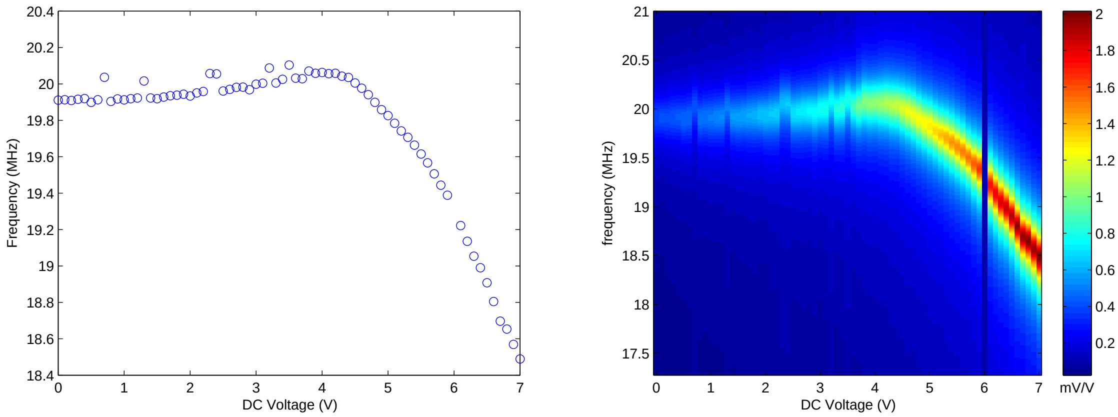

(a) (b)

Figure 4.1.6: The parameters obtained by fitting the data to the simple harmonic oscillator model can be used in several ways, of which two are shown here. Figure 4.1.6a uses the resonance frequency parameter and shows its relation to the DC voltage. The reconstructed 3D colourplot of the dataset presented in figure 4.1.4 can be seen in figure 4.1.6b.

As can be seen in these two graphs, the SHO model does not always provide an accurate fit of the data, so for those traces, the provided output parameters are set to NaN values. In the case of this dataset, the frequency spectrum taken at a DC voltage of 6.0 V could not be fit to the model, hence the jump in the relation between the resonance frequency and the voltage in figure 4.1.6a. Also, there is one peak missing in the colourplot in figure 4.1.6b for this reason, creating a disruption in the plotted magnitude amplitude.

Four more parameter values follow from the data processing, the Q-factor, the maximum amplitude, the cross-talk and the noise floor. The focus is mainly on the These values are calculated when the data is fitted to the model and can give insights to the behaviour of the drum. The Q-factor shows how well the mechanical resonator can operate at specific frequencies and how much it is influenced by dissipation in the resonator by examining the peak width in relation to the resonance frequency. Observing the maximum amplitude is often done after fitting the data to the SHO model. It would be more favourable to obtain the maximum amplitude of the data itself if that would give accurate information, but that is unfortunately not possible due to the noise peaks that occur in the frequency spectrum. These have higher amplitudes than the actual resonance amplitudes, so when looking at the maximum amplitudes of the raw data, noise peaks would cause outliers in all analyzed parameters. Even when selecting a certain range of data to fit to the SHO model, there are often noise peak in the frequency range that is of interest when fitting. Therefore often the fitted amplitude is analyzed and the maximum amplitude of the fitted frequency spectra are used to acquire information about the behaviour of the resonator instead of the raw data. The following graphs show the Q-factor and the maximum fitted amplitude, again plotted as a function of the DC voltage.

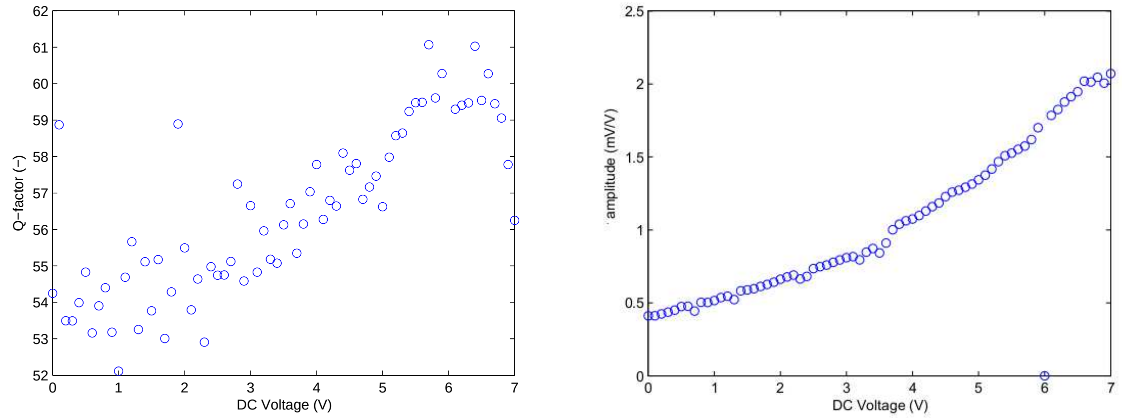

(a) (b)

Figure 4.1.7: Two more parameters obtained by fitting the data to the simple harmonic oscillator model. Figure 4.1.7a shows the relation of the Q-factors of each peak to the DC voltage. The maximum amplitude of each frequency spectrum as a function of the DC voltage can be seen in figure 4.1.7b.

These plots show that even though the amplitude of the signal increases almost linearly with the applied DC voltage, it is difficult to see the same relation in the Q-factor. The typical value of Q-factors around 50 for devices similar to the one measured here remains within 15% of its initial value. When investigating how the Q-factor changes when applying DC voltages to the sample a fit can be made, but when applying a linear fit and a quadratic fit to this plot, it provided similar variances, meaning no conclusions can be drawn.

4.1.3. INITIAL SAMPLE PROBLEMS

Several measurements showed in the previous sections promising electrical actuation and DC frequency tuning results with the initial sample, but there are also numerous measurements that show problems occuring with the initial sample. First, the frequency tuning is plotted in figure 4.1.8. It is driven electrically and tuned up to higher voltages, from 0 V to 12 V, again with a 0.1 V step size.

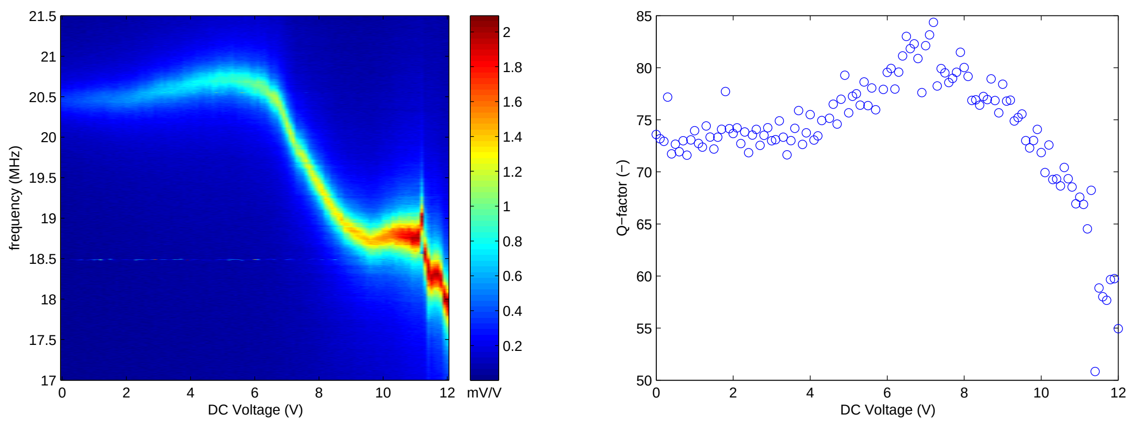

(a) (b)

Figure 4.1.8: The first indications of the limitations of the initial sample become clear when trying frequency tuning up to higher voltages.

Figure 4.1.8a is a plot of the magnitude, following the same trend as figure 4.1.4a, but quickly becomes unstable and starts to show unpredictable behaviour. The drum appears to be unaffected by an increasing DC voltage from 9 V to 11 V and starts moving up and down in resonance frequency from 11 V to 12 V. This change in behaviour is also observable in the resonance frequency, which gradually drops from 9 V to 11 V and returns NaN values for several frequency spectra between 11 V and 12 V because it's impossible to fit the spectra to the SHO model.

The graphs above show that the drum presented in the previous section begin to change its behaviour as the DC voltage is increased above 9 V. The magnitude shown in figure 4.1.8a again shows the decrease in resonance frequency, but now shows that when increasing the DC voltage past 7 V, it appears to not affect the resonance frequency any further. The most likely explanation for this behaviour requires a closer look to the geometry of the system. The membrane is suspended over a ciruclar hole and is attracted to the gate of the substrate due to the applied DC voltage as explained in section 2.3. This means the drum is streched, while remaining clamped at the edge of the circular hole it is suspended over. When looking at a one dimensional perspective to simplify the geometry, the electrostatic force causes a change in the membrane length, as shown in figure 4.1.9.

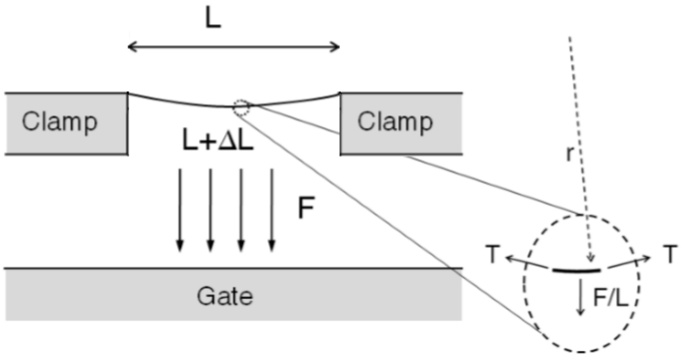

Figure 4.1.9: Schematic overview of a fully clamped membrane simplified to one dimension. The electrostatic force **F** causes a change in the length **L** of Δ **L**. **T** is the longitudinal tension in the membrane and r is the radius of curvature of the membrane deflection. Adapted from Chen [8].

Streching the membrane is only possible to a certain extend. Graphene can be streched over 10 %, meaning it can stretch quite far as a result of the electrostatic force. However, the model described above assumes that the membrane is perfectly clamped. This neglects the possibilities that the flake starts to slip and move in the in-plane direction. When pulling the membrane with both the DC voltage and the RF modulated voltage, the amplitude at which the distance between the membrane and the gate is minimal, the force on the membrane might cause it to slip and become slightly detached from the sample surface as soon as it returns to the highest amplitude caused by the RF voltage. Then, when setting another DC voltage the membrane can become reattached or detached slightly further, causing the resonance frequency to shift up and down. The adhesion of the flake to the surface of the sample could be improved by using different materials as gate and membrane. A much more serious problem with the initial sample is the build up of charge due to the large parasitic capacitance, as explained in section 3.1.3. The experiments to verify the charging effects that occur due to this large capacitance are discussed in the following section.

4.1.4. HYSTERESIS AND CHARGING

To test if a build up of charge occurs in the sample, a sweep of the DC voltage is made, where the resonance frequency response is measured as a function of DC voltage. By sweeping from 0 V to a certain positive voltage and back down to 0 V, possible hysteresis can be observed, by comparing the frequency tuning at the same frequencies on the upward and downward sweeps. Hysteresis is expected to occur due to the build up of charge. The data obtained from these upwards and downwards sweeps are processed in the same way as the results described in the previous section, showing the magnitude and phase data in the frequency spectrum as a function of the DC gate voltage applied on the samples together with the RF voltage that drives the drums resonance.

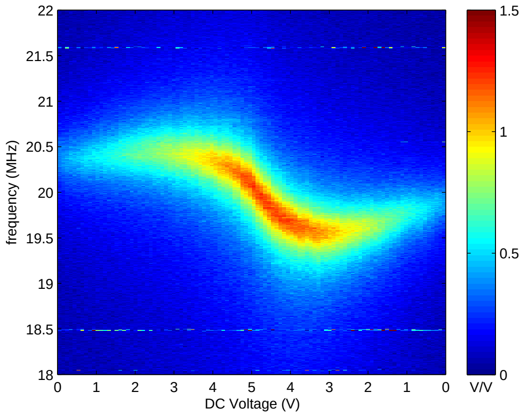

(a)

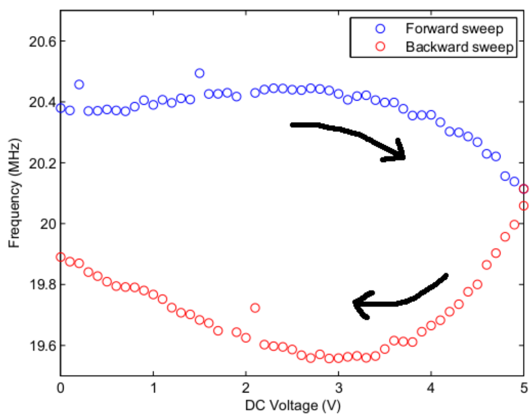

(b)

Figure 4.1.10: When sweeping the DC gate voltage to 5 V and back to 0 V, it is obvious that there is large hysteresis present. The resonance frequencies for DC voltages on the backwards sweep are far from similar to the ones measured on the forward sweep. Figure 4.1.10a shows the magnitude in a colourplot, figure 4.1.10b presents the fitted resonance frequencies as a function of DC voltage.

When observing the results shown in figure 4.1.10, it can quickly be concluded that there is a tremendous amount of hysteresis, most likely caused by charging of the sample. The fitted resonance frequencies keep decreasing after the the DC voltage starts to ramp down, indicating a further build up of charge and therefore more electrostatic spring softening and a decreasing resonance frequency. Several more measurements show the exact same result. Another quick check was done by quickly increasing the DC voltage and then taking measurements when sweeping the voltage down from a certain voltage and back up to the same voltage after reaching 0V. In the graphs below, sweeps to 8 V are compared. At first, the same sweep direction as figure 4.1.10 is used, from 0 V to 8 V and back to 0 V in steps of 0.1 V. Secondly, the DC voltage is started at 8 V, goes down to 0 V and back up to 8 V, with the same step size.

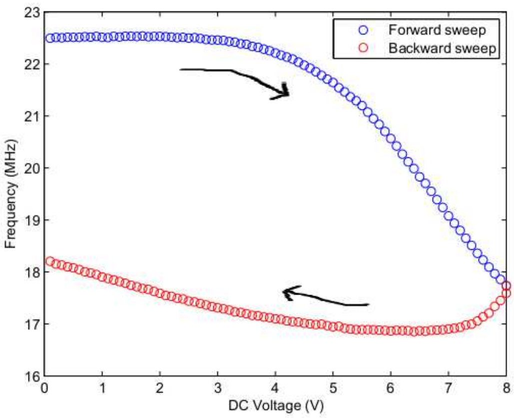

(a)

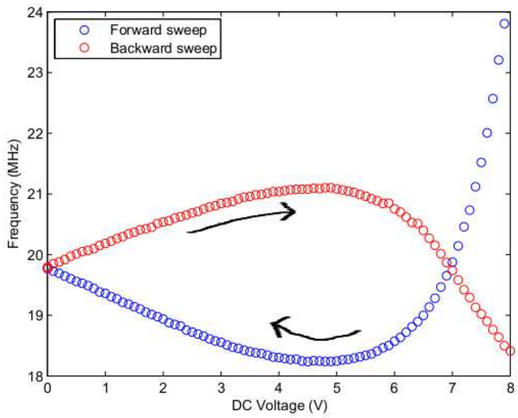

(b)

Figure 4.1.11: The fitted resonance frequencies as a function of DC voltage show the hysteresis clearly. Note that figure 4.1.11a shows the DC voltage sweep initiated at 0 V, increased to 8 V (blue data points, from left to right) and decreased back from 8 V to 0 V (red data points, from right to left). Figure 4.1.11b shows the measurement starting at 8 V, decreasing to 0 V (blue data points, from right to left) and increasing from 0 V to 8 V as the backward sweep (red data points, from left to right).

A solution for the hysteresis problem would be to take measurements with long time intervals between each measurement. The capacitors in the sample would be able to discharge and the effect of trapped charges minimized. This is showed when measuring with 1 minute intervals between each 0.1 V step.

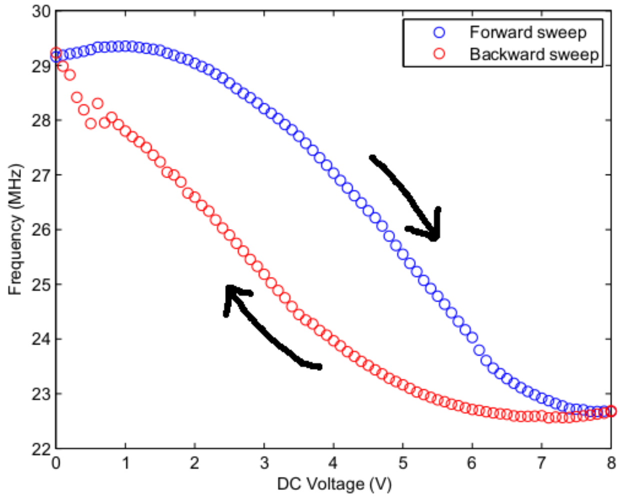

Figure 4.1.12: Fitted resonance frequency as a function of DC gate voltage when a 1 minute interval is taken between each 0.1 V step. All other settings are the same as the measurement shown in figure 4.1.11a.

The graph above shows that the difference between the measured resonance frequencies is smaller than without the time interval of 1 minute (so comparing figure 4.1.11a and 4.1.12a). The charge trapped in the sample is able to slightly diffuse and cause less hysteresis.

Upon further investigation of the design, a possible reason for the build up of charge was not only due to the large parasitic capacitance, but also due to the oxidation of the top metal layer. The convenience of leaving the chromium on the sample as a conductive top gate also became a problem, since the chromium oxidizes in ambient conditions. This oxide layer on top of the chromium forms another capacitor, as shown in figure 4.1.13.

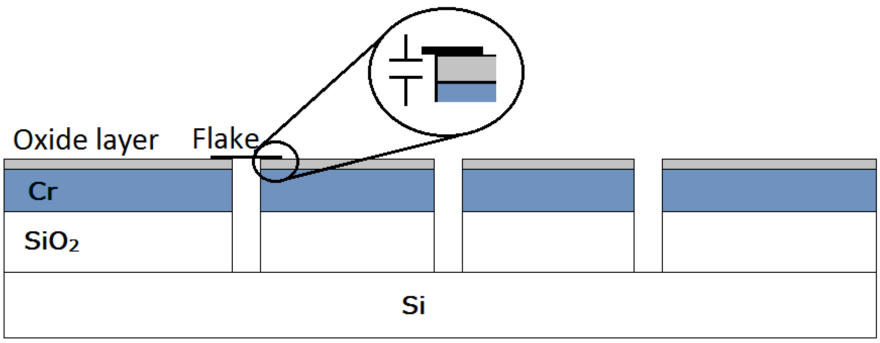

Figure 4.1.13: Schematic overview of capacitance between flake and oxidized chromium. The 30 nm chromium layer oxidizes to form an oxide layer of several nanometers. The flake of also several nanometers thick acts as the second conducting layer of the capacitor.

Both the oxide layer and flake are of the order of several nanometers thick, but are large enough to form a small capacitance. This capacitance can be estimated using the equation $C_g = \frac{\varepsilon_0 \varepsilon_R A}{d}$. The electric constant ε_0 is approximately $8.854 * 10^{-12} F/m$, the dielectric constant ε of chromium oxide is 13, let's assume the thickness of the chromium oxide is 2 nm and the surface area is estimated as approximately $1.5 * 10^9 \mu m^2$. This means the capacitance between the flake and the surface of the substrate is 85 pF, so in the same order of magnitude as the parasitic capacitance between the chromium surface and the silicon back gate. This is the reason that the metal gate was changed from a chromium layer to a gold palladium layer.

Even though the results shown do not follow generally predicted models or are useable as data to develop a model predicting the behaviour of electrically driven drums, several useful conclusions are drawn from the processing of the results, such as what parts of the fabrication of samples needs to be changed or improved and how to process the data obtained from the setup. The changes in fabrication are explained in section

3.1.2 through 3.1.4 and the programs written to analyze the data are used in the following sections to process the measurement data of the improved samples.

4.2. ELECTRICAL DRIVE OF IMPROVED SAMPLES

After the adjustments to the fabrication method were made, creating new substrates, several new flakes were stamped over the holes in the new pattern. To investigate possible differences in frequency tuning behaviour, both MoS_2 and graphene flakes are stamped on the improved samples. To also test the assumption made in the model that certain tuning characteristics depend on the bending rigidity of the suspended membranes, drums of several thicknesses are made by stamping flakes of different thicknesses on the improved samples. The figure below shows an overview of the different samples used to do measurements on.

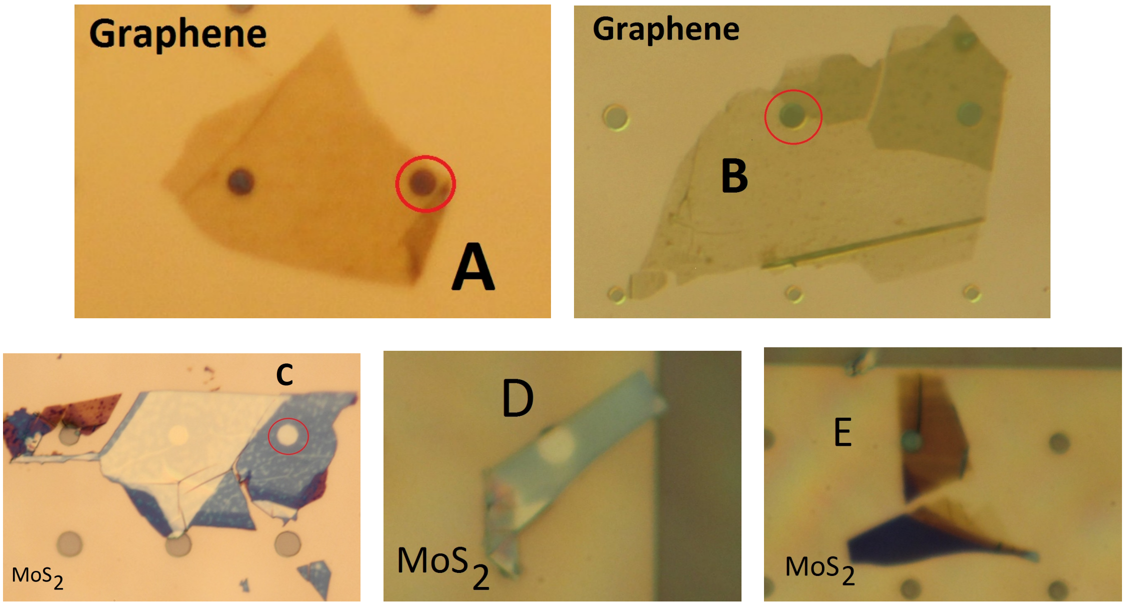

Figure 4.2.1: Five different samples were measured, of which 2 flakes are graphene and of which 3 are MoS_2. The flakes are stamped so that membranes are suspended over circular holes which are 150 nm deep. The yellow contact area is a gold palladium surface, connected to a bond pad to make electrical connections. When several holes are covered by the flake, a red circle is added to the image to indicate the drum that measurements are done on.

These five samples will from now on be refered to as sample A, B, C , D and E where figure 4.2.1a is sample A, figure 4.2.1b shows sample B, figure 4.2.1c sample C, figure 4.2.1d is sample D and figure 4.2.1e is sample E. All suspended membranes have different properties, since they are made of different materials, have different thicknesses and are suspended over holes with different diameters. Thicknesses are measured with an AFM and all properties are summarized in the following table.

Table 4.1: Properties of the 5 samples shown in figure 4.2.2

Figure	Sample	Material	Drum diameter (μm)	Drum thickness (nm)
4.2.1a	A	Graphene	3	7
4.2.1b	B	Graphene	3	5
4.2.1c	C	MoS_2	4	17
4.2.1d	D	MoS_2	4	6
4.2.1e	E	MoS_2	3	8

All these samples have shown a better signal to noise ratio in the resonance frequency spectra as the initial sample discussed in section 4.1.

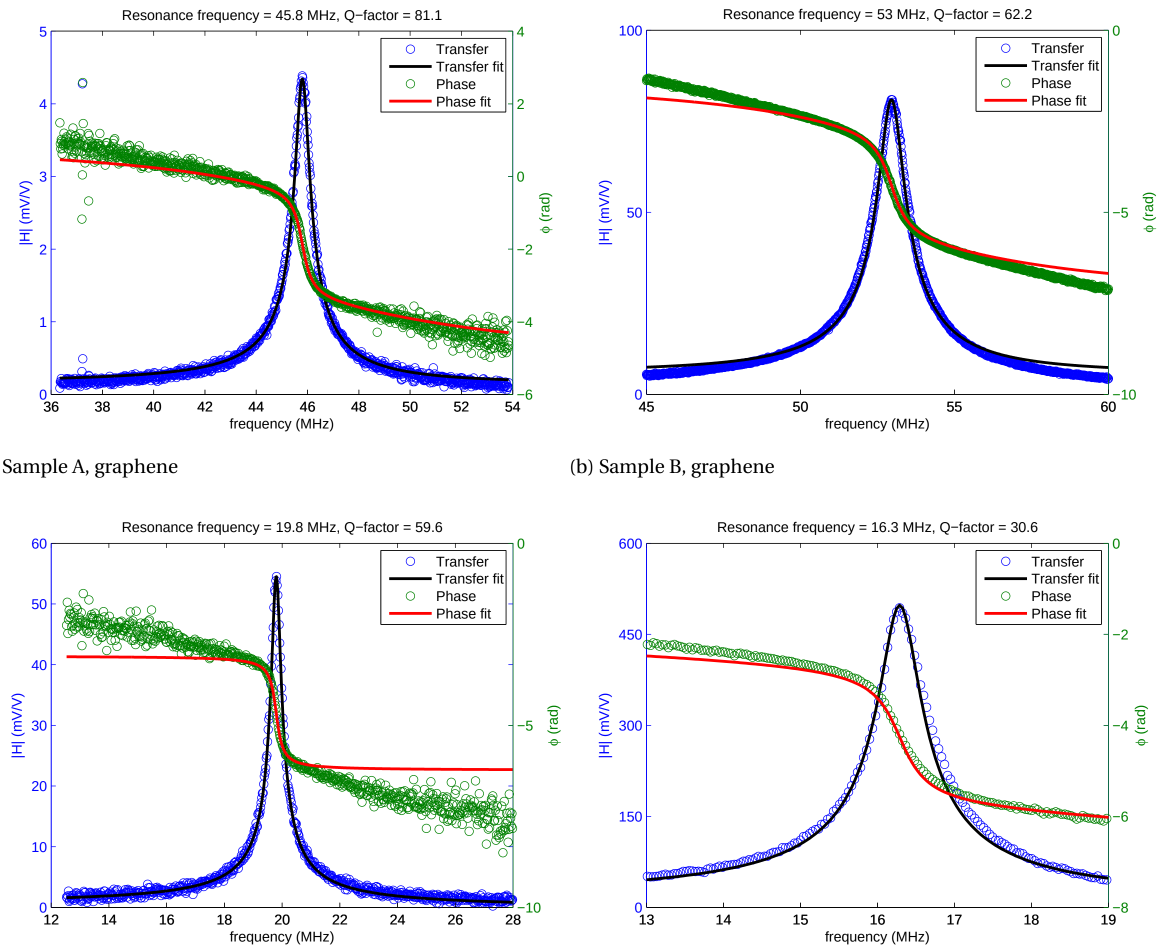

(a) Sample A, graphene

(b) Sample B, graphene

(c) Sample D, MoS_2

(d) Sample E, MoS_2

Figure 4.2.2: Out of the five samples, these four graphs most accurately represent the behaviour of the drums that are made with the improved fabrication method. The signal to noise ratios are better than in the initial sample of figure 4.1.3 in both magnitude and phase data. The improvement of the drum behaviour using electrical drive is promising when further investigating the drum behaviour through DC tuning. Note that even though the phase values might be different for each drum, the phase change at the resonance frequency is always π.

4.2.1. REDUCTION OF HYSTERESIS

The large amount of hysteresis found in the initial sample, as shown in section 4.1.4, is not detectable in the improved samples. When observing the resonance frequency tuning graphs, the backwards trace almost completely overlaps that of the forward sweep. Figure 4.2.3 shows an example of the magnitude of one of the improved samples, together with the resonance frequencies tuned by the applied DC gate voltage and fitted to the SHO model. The data presented in sections 4.2.1 and 4.2.2 is taken from measurements of sample A.
It is visible in these graphs that there is very little to no hysteresis in the improved samples. The resonance frequency is equal for the same DC values when sweeping the DC voltage upwards and downwards. This means that any possible charging of the sample due to parasitic capacitances is negligible and does not affect the frequency tuning or the electrical drive of the samples. According to the theory, providing a negative DC voltage should provide the same results. More specifically, the amplitude of the deflection scales with the DC voltage squared, so the positive and negative voltages with the same value should provide the same deflection and thus frequency tuning. The polarity of the voltage applied to the gate is therefore reversed and the measurement is repeated. The results are identical, as can be seen in the graphs below.

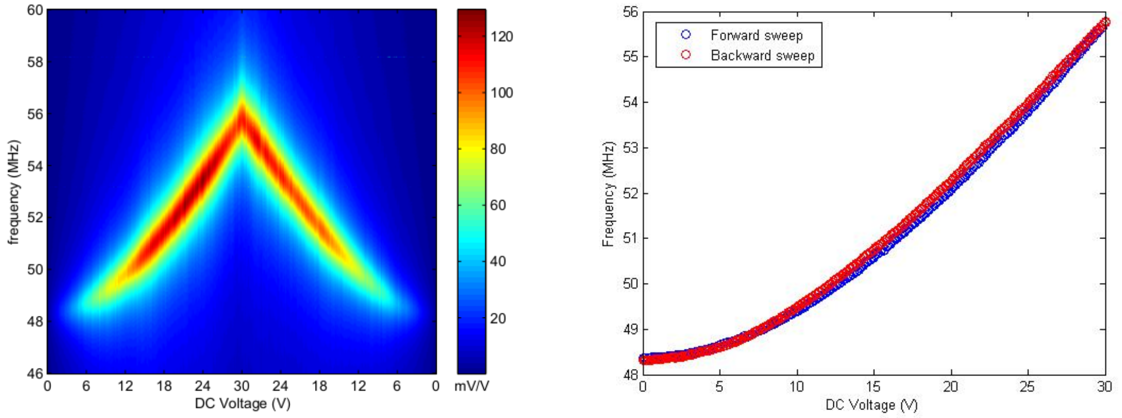

(a) (b)

Figure 4.2.3: The magnitude and especially the traces of fitted resonance frequencies show that the hysteresis is almost completely gone when applying a DC voltage on the improved samples. Also note that the frequency spectra for DC voltages up to 30 V remain linear and show predictable behaviour.

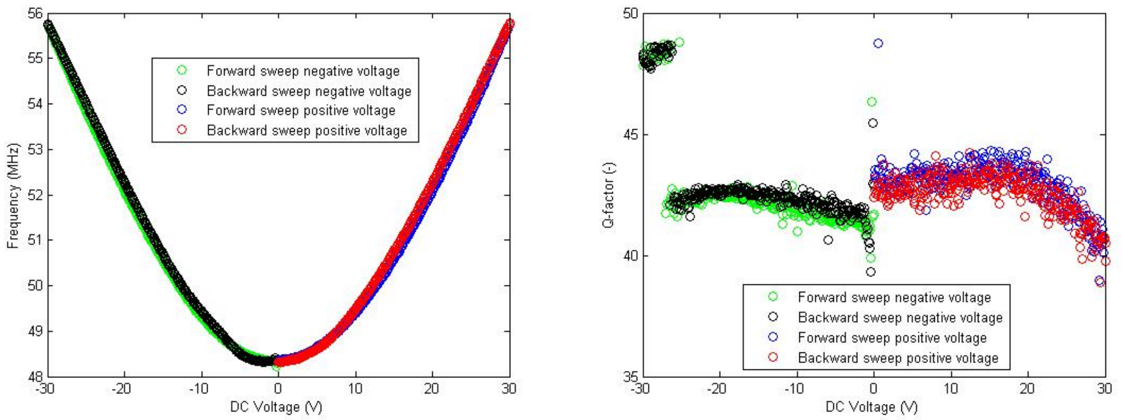

(a) (b)

Figure 4.2.4: Plotted are the fitted resonance frequency values and Q-factors for each negative and positive DC voltage. The graphs are combined plots of two measurements, a forwards sweep from 0 V to -30 V and back and a second measurement from 0 V to 30 V and back. Note the similarities in resonance frequencies and identical range of Q-factors. The only difference is the sudden jump in Q-factor around -28 V, for which no explanation has been found yet.

4.2.2. FREQUENCY TUNING RESPONSE

The response of the drums to a set DC voltage is also improved significantly. Figure 4.1.12 show that even with a wait time of 1 minute between each measurement there is still significant hysteresis, but the improved samples shows an instantaneous respons to changes in the DC voltage. Even step sizes of 1 V are no problem and no hysteresis occurs, as can be seen in the following figure.

The fact that there is no hysteresis, even when taking steps of 1 V (and every measurement takes 3 seconds), indicates that the response of the drum to an electrical signal has significantly improved. This not only means that possible trapped charges will be negligible and frequency tuning will have a larger effect, but it also indicates that electrically driving the mechanical resonance shows potential as a method to investigate suspended membranes. Changes in other parameters such as pressure and mechanical strain will be possible while the drum remains properly actuated by the electrical signal.

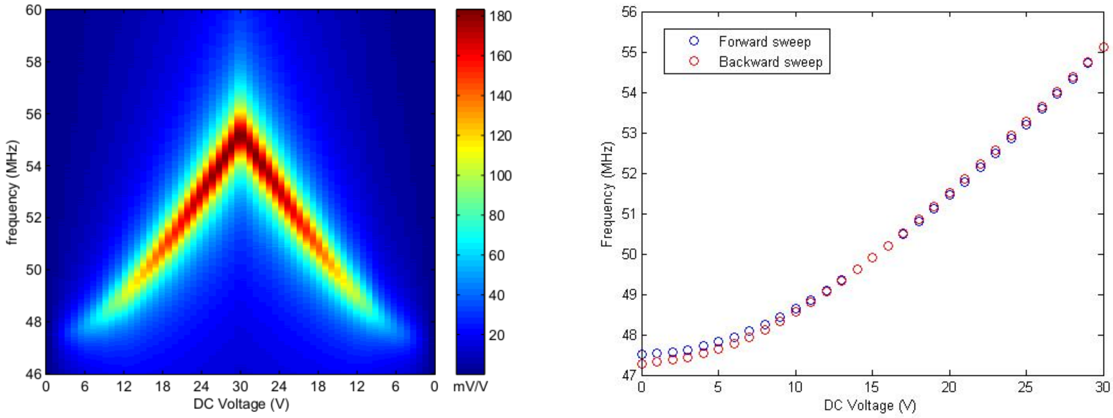

(a) (b)

Figure 4.2.5: The magnitude data in figure 4.2.5a shows the same trend as figure 4.2.3 and figure 4.2.5b comfirm there is still no hysteresis in these samples, even when taking a larger step size when sweeping the DC voltage.

4.3. FREQUENCY TUNING

After showing the possibility and accuracy of electrically driving a suspended membrane to achieve a mechanical resonance, the next step of these devices is to investigate how accurately and in what range it is possible to tune the frequency of the drum. Since this thesis focusses on using electrical signals, a combination of a RF modulated voltage and a DC voltage is used to respectively drive and tune the drum. This section explains how this affects the amplitude of the mechanical resonance and if any differences occur between positive and negative voltages and if the change is polarity of the DC tuning voltage (section 4.3.1), in what range the resonance frequency can be tuned (section 4.3.2 and finally whether the results obtained from measurements agree with the proposed model in theory section 2.3 (which can be found in section 4.3.3).

4.3.1. INCREASE IN AMPLITUDE DUE TO FREQUENCY TUNING

As was shown briefly in section 4.1.2, the amplitude of the mechanical resonance increases when increasing the DC voltage used to tune the frequency when using the electrical actuation. In all other magnitude graphs so far, it is observable that for increasing DC voltages (or better yet, when the absolute value of the DC value increases), the amplitude of the drums resonance increases. The theory as mentioned in section 4.1.2 is that electrostatic spring softening causes the drum to resonate at lower frequencies and also causes an increase in amplitude. This would mean that when electrostatically tuning the resonance frequency downwards, an increase in amplitude should be visible. When going past the electrostatic spring softening regime, the amplitude should decrease again as the resonance frequency increases by the induced strain. This phenomena is independent of the actuation method and should only be affected by the frequency tuning. For measurements shown in previous figures, this is the case. However, these graphs are all processed from data that used the electrical actuation method to drive the mechanical resonance and only show electrostatic spring softening. Measurements using the optical actuation, while still electrically tuning the drum with the DC voltage, should show the same behaviour.

When comparing the the two actuation methods with the same sample and DC tuning, conclusions can be drawn about the resonator amplitude as a function of the electrical drive signal as stated above. Therefore, several measurements are done directly after each other using the same DC voltage sweeps and only changing the actuation method from electrical to optical and vice versa. Driving powers of the two methods are set by experimentally investigating the regime in which the membrane behaves linearly and similar frequency tuning behaviour is observed. Two samples are investigated in this way, samples C and D. Again, the data is fit to the SHO model and now the resonance frequency, Q-factor and maximum amplitude of the fitted signal are plotted as a function of the DC tuning. As explained earlier, using the fitted amplitude and other parameters to analyze the data is done to rule out any noise peaks present in the measurement data that might have higher amplitudes that the resonance frequency peak that is relevant. These peaks do not occur in the fitted resonance frequency spectra, so they provide a clear understanding of the amplitude of the resonance peaks after fitted by the SHO model. The disadvantage of this method is that not all data is used, since some frequency spectra do not converge to fit the SHO model and these data points are removed from the fitted maximum amplitude plots. However, it is more important to have correct data than it is to have more data points, since the focus is mainly on the qualitative behaviour of the resonator amplitude.

Unfortunately, results from sample D are not very usable, since the fitting program was not able to find fitting resonance curves for many DC voltages. This means approximately 70 out of 280 data points can be used to investigate the amplitude behaviour (the DC voltages are again increased with steps of 0.1 V and the DC range is 1-15 V, hence 280 data points). The trend of the magnitude, the Q-factor and the maximum fitted amplitude can be seen in figure 4.3.1 for both electrical and optical actuation. Although the data set does not provide conclusive results, it does represent the general behaviour that is seen in more resonators.

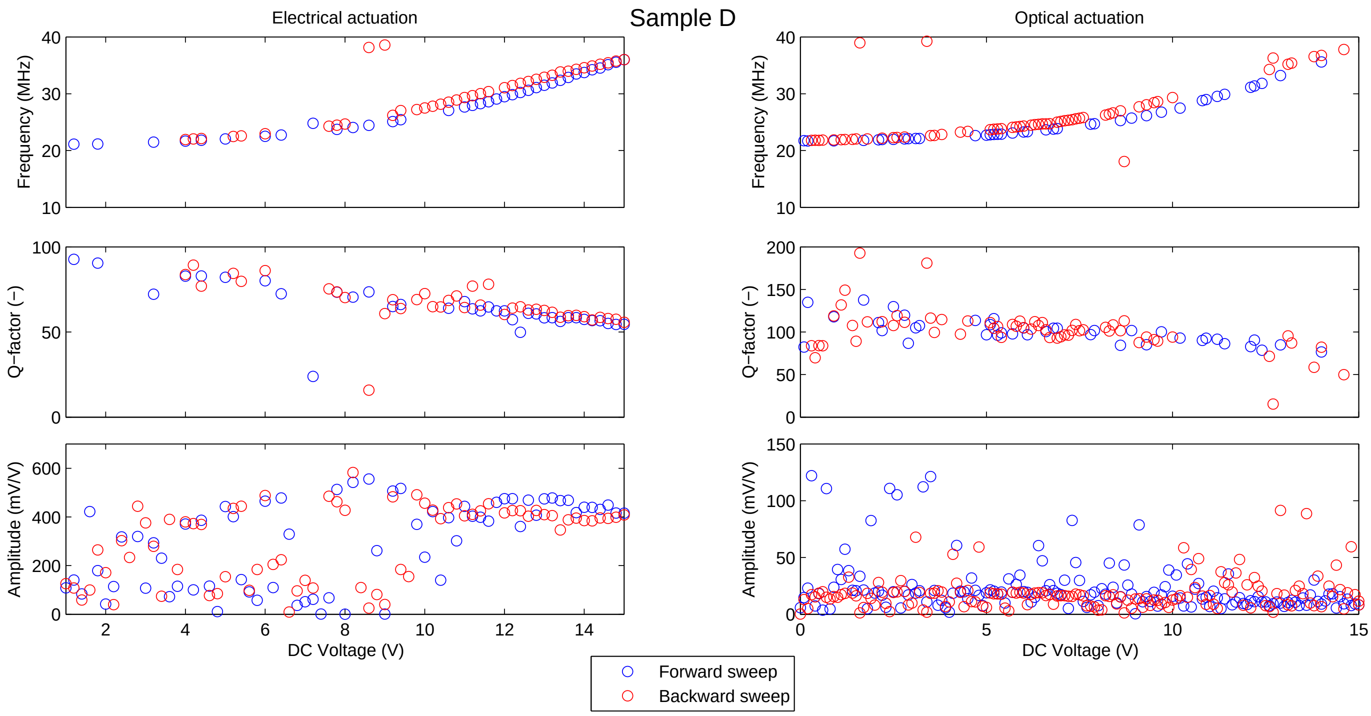

Figure 4.3.1: Comparison of electrical and optical actuation when only changing the DC voltage in sample D. On the left is the data from the electrically actuated drum. On the right is the data obtained when using optical actuation. Most important are the two bottom figures. These show the fitted maximum amplitude of each resonance frequency spectrum shown as data points in the magnitude graph. As can be seen, the electrical actuation does not show a clear increase, but is of an order of magnitude larger than the values seen in the optical actuation plot. A steady high value between 400 and 500 mV/V for high DC voltages show that the maximum amplitude is dependent on the DC voltage. However, the increase does not appear for increasing voltages in the optical actuation graph, which remains steady at 20 mV/V on average, showing the amplitude increase is an effect of the combination of electrical actuation and DC tuning. The top two figures show the magnitude graphs of the electrical and optical actuation, plotting the resonance frequency as a function of DC voltage. The tuning curves show very similar resonance frequencies at a range of DC voltages, indicating that DC tuning is independent of actuation method. The Q-factor plots, which are the middle two plots, appear to confirm this. Their dependancy on the DC voltage is similar, with a decrease in both, from 90 to 60 for electrical actuation and from 120 to 90 for optical actuation.

Even though sample D does not distinguish the differences between optical and electrical actuation, it is obvious from figure 4.3.1 that the resonance frequencies and Q-factors of the sample are similar for both actuation methods. A comparison between the fitted amplitudes for the two actuation methods shows a remarkable and clear difference. The optical actuation shows a steady amplitude, where the resonance peak reaches 20 mV/V on average and is not dependent on the DC voltage applied to tune the resonance frequency. Although it is not completely obvious how the amplitude the DC voltage are related in both these figures, there is an apparent relation between the DC voltage and amplitude for electrical actuation. The amplitude is an order of magnitude larger than the amplitudes for optical actuation, ranging from 100 mV/V to 500 mV/V. Although the spread is too large to draw any conclusions from this data, it is surprising to see that the amplitude increases at higher DC voltages. There is no apparent electrostatic weakening and the frequency tuning appears to only be determined by the added strain in the drum, which intuitively would cause a lower amplitude as explained in section 4.1.2. It can be concluded that the there are more factors influencing the amplitude than just the resonance frequency. The driving force is most likely one of these factors, as it increases as a function of DC voltage, as can be seen in equation 2.18. A more thorough explainantion will follow after figure 4.3.2, where there are more well defined plots of the same three parameters as in figure 4.3.1: the resonance frequency, the Q-factor and the amplitude.

The results from sample C are more conclusive. The frequency tuning curve is slightly different and the sample is now tuned with a DC voltage sweeping from a negative voltage to the positive voltage (through 0 V, still in steps of 0.1 V), but for the amplitude comparison the focus will simply be on the similarities in frequency tuning and Q-factor and the differences in fitted maximum amplitude. The same plots as in figure 4.3.1 are shown in the following figure for sample C.

When looking at the data presented in figure 4.3.2, we can conclude that the two actuation methods indeed do have different amplitudes when the frequency is tuned by a DC voltage. However, all graphs show a symmetry around 0 V, such that all data for negative DC voltages are similar to that of an equally large positive DC voltage. Therefore, from now on, observations made about any parameter as a function of DC voltage will be assumed to behave in the same way for positive DC voltages and equally large negative DC voltages unless indicated otherwise. The fitted maximum amplitude clearly increases significantly as a function of increasing DC voltage when the drum is actuated electrically as visible in the left hand side amplitude graph in figure 4.3.2 (blue). On the contrary, there is very little difference in the amplitudes at different DC voltages when actuating optically, indicated by the right hand side amplitude graph (red) in figure 4.3.2.

The small changes in amplitude for the optical actuation method could be due to the change in position of the membrane in respect to the back mirror of the interferometer. A slightly more favourable distance between the first and second mirror can change the interference between the two reflecting laser beams used to probe the membrane, causing a small change in the magnitude data. It is hard to quantify this change, because it is unknown how far the drum is pulled towards the gate by the DC voltage and therefore exactly how much this affects the interference of the laser that probes the membrane motion.

It is clear the change in interference can not be the explanation for the increase in amplitude when actuation electrically and tuning with a DC voltage. If it would be, the shape of the maximum amplitude as a function of DC voltage would be more sinusoidal or at least periodic in shape. Also, the difference in amplitude would not be as large as it currently is. When carefully observing the dependence of the amplitude on the DC voltage, the blue amplitude graph in figure 4.3.2 shows a very low amplitude of less than 10 mV/V for DC voltages below 2 V. The amplitude then rapidly increases to 225 mV/V in a DC voltage increase from 2 V to 5 V. From there on, when the DC voltage increases further from 5 V to 10 V, the amplitude seems to steadily increase to a further 250 mV/V. Again it is concluded that there must be an electrical mechanism that causes the increase in amplitudefor electrical actuation as the amplitude when using optical actuation does not appear to change as a function of DC voltage.

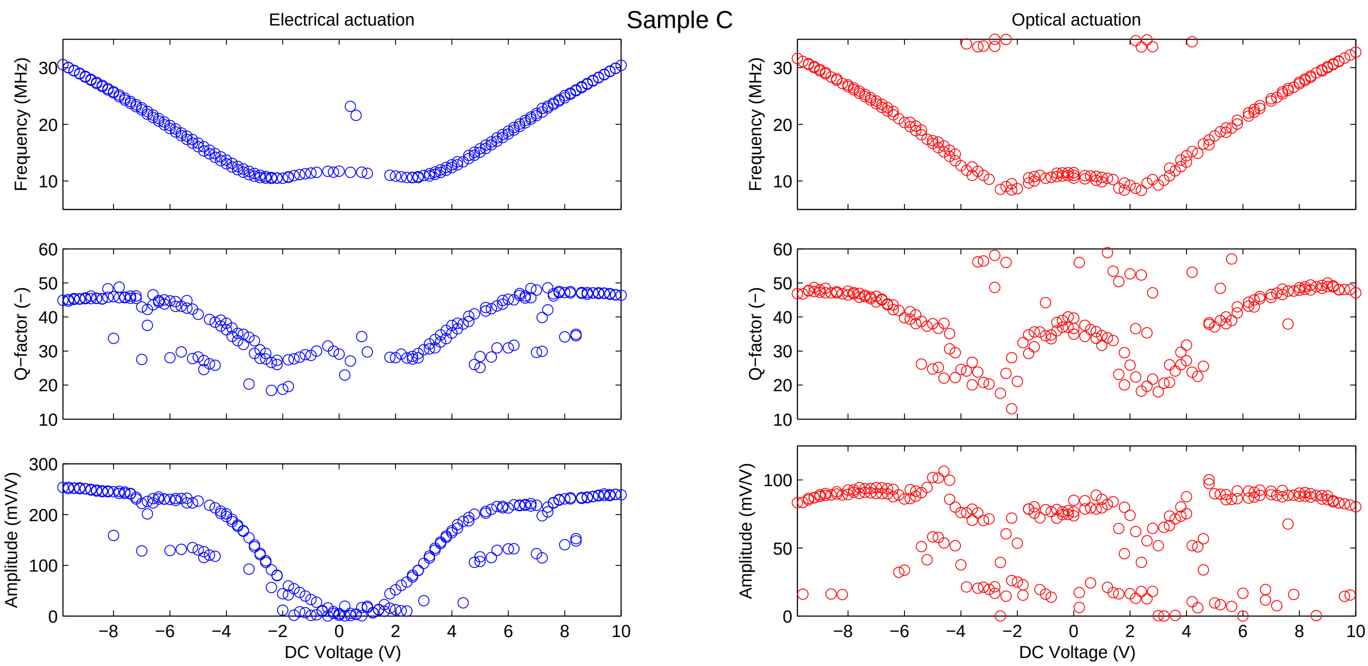

Figure 4.3.2: Comparison of electrical and optical actuation when only changing the DC voltage in sample C. Similar as in figure 4.3.1, the blue data points in the left figures show the data obtained from the electrically actuated drum. In red, the figures on the right, the data from the optically actuated drum is presented. Most important are the amplitude graphs, which are the two bottom figures. These show the fitted maximum amplitude of each resonance frequency spectrum shown as data points in the magnitude graph. Sample C shows a more obvious trend, the amplitude increases for electrical actuation with increasing DC voltage. Positive and negative DC voltages show the same trend. Optical actuation does not show a large increase in amplitude, but there is some variation in the amplitude around -4 V and 4 V, which could be due to fitting difficulties. The maximum amplitude decreases somewhat below -7 V and above 7 V in similar ways, but this effect can not be explained thus far. When observing the frequency tuning graphs inthe top two figures, the tuning is very similar for the two different actuation methods. More interesting are the Q-factor graphs in the middle figures, which are somehow dependent on the frequency.

As discussed in section 2.2, the electrostatic force applied to a membrane when applying a DC and AC voltage is given in equation 2.18. The amplitude of the AC voltage, in this experiment the RF modulated voltage, is kept constant during all experiments and only the DC voltage is changed. Expected is that the electrostatic force therefore increases quadratically with DC voltage, as indicated by the first term in equation 2.18, with a linear dependence added to it due to the second term in the equation. The amplitude is expected to follow the quadratic behaviour, because that is the only time varying component affecting the resonance. However, this is not observed clearly. The quadratic dependence of the amplitude can be seen for DC voltages ranging from 0 V to 5 V, but after that it continues to increase, but not quadratically. The most likely explanation is that there is a change in the device where the membrane either starts to slip or drift, meaning the adhesion to the edge becomes less. This would explain that the measurement data follows the theory up to a certain DC voltage.

To really draw accurate conclusions about the dependence of the resonator amplitude as a function of DC voltage, more samples are needed that clearly show a quadratic relationship, after which the theory can be fit to the experimental results. Although the results in this section do seem to confirm that theory, they are not conclusive. A test that would need to be done in order to rule out any possibility of the electrical RF signal influencing the amplitude increase would be to measure the amplitude at different DC voltages while keeping the product of the DC and RF voltages constant. This would remove the linear increase cause by the first term in equation 2.18 because it remains constant and the electrostatic force acting on the drum will only change as a function of DC voltage.

4.3.2. FREQUENCY TUNING RANGE AND SENSITIVITY

An important parameter when discussing frequency tuning is the range in which the frequency of a device can be tuned. When a certain resonance frequency has a corresponding Q-factor that is around 100, which is found to occur quite frequently for room temperature devices, it means that there is a certain width of the resonance peak that causes a uncertainty. When the frequency tuning is in the same order of magnitude of the uncertainty, there is little use for the MEMS device, as the frequency tuning can not be used to generate or detect out specific frequencies, which would be the goal for these devices. Therefore, a large part of the measurements done during this thesis is done to investigate the different tunabilty ranges of different devices.

There are two types of frequency tuning, positive frequency tuning and negative frequency tuning. Positive tuning means that spring stiffening occurs as an effect of an increased DC voltage, such that the resonance frequency increases. This is mainly due to the induced strain in the drum when it is being pulled towards the gate by the DC voltage. Negative tuning is the opposite, where spring weakening occurs due to the electric field, causing a decrease in resonance frequency when the DC voltage increases. In fact, when neglecting bending rigidity in drums, both negative and positive frequency tuning occur in all devices, the smallest change in DC voltage induces a small electrostatic spring weakening, thus negative frequency tuning. For higher DC voltages, the added strain due to the drum being pulled towards the gate starts to induce positive frequency tuning. In what range of DC voltages negative and positive frequency tuning occur is determined by the initial conditions of the device, most importantly the built-in strain and the effective mass of the drum. Firstly, both seperate cases of negative and positive frequency tuning will be investigated, after which a combination of both will be presented. The next section explains how these measurements fit the model proposed by Chen [37].

As mentioned in section 2.3, the initial conditions of the sample determine the amount of negative and positive frequency tuning. Only positive tuning occurs in samples with low built-in strain, as already visible in figure 4.2.3, where sample A is measured. The suspended flake appears to have a low built-in strain, as there is no trace of any negative frequency tuning. Similarly, sample D shows only positive tuning when observing the data presented in figure 4.3.1. The amount of frequency tuning can be taken over several ranges, as the frequency does not scale linearly with the applied DC voltage. In most cases, the maximum slope of the frequency as a function of DC voltage will be given, as this is the maximum frequency tunability.

The data set of sample A shown in figure 4.2.3 shows a rather low tunability, where the resonance frequency is tuned from 48.3 MHz to 55.8 MHZ, so a tuning range of 7.5 MHz when tuned with a DC voltage range of 0 V to 30 V. The maximum tuning sensitivity in this device is 0.44 MHz/V, which is slightly disappointing. The advantage of sample A is the responsivity, showing there is little build up of charge in the sample.

When calculating the same values for sample D, shown in figure 4.3.1, a much more impressive tunability range of 17.5 MHz over 15 V is found, with a maximum tuning sensitivity of 4.51 MHz/V. This is closer to the maximum value found by Chen *et al.* [12], who claim to have measured tuning sensitivities of up to 8 MHz/V.

Another sample that showed only positive frequency tuning is sample E. After previous results, sample E showed a quite remarkable tunability range. At first glance, it seemed to be a great sample, where the resonance frequency started at 25 MHz and went up to more than 75 MHz when tuning from 1 V to 15 V. This would mean a tuning range of 55 MHz and large tuning sensitivities. The magnitude graph and resonance frequency tuning graph can be seen in figure 4.3.3.

Upon closer inspection, there appears to be a split resonance peak during parts of the tuning curve. It is visible in the magnitude graph in figure 4.3.3a that when the DC voltage is between 1 V and 10 V, there is not one clear resonance peak, causing problems in fitting the data to the SHO model. When looking at the data in figure 4.3.3b, the resonance frequency is not always accurately obtained. The data from 10 V and higher does seem reliable, so observing the frequency tuning in this range, a tuning sensitivity of 5.28 MHz/V is found. The sensitivity between 8 V and 9 V is 6.58 MHz/V, but this range of DC voltage shows unpredicatble results, so is not to be trusted. The tunability range in total is 52.7 MHz for DC voltages going from 1 V to 15 V. Unfortunately, these results are not reproducable in any other samples. The explanation for the peak splitting is possible a wrinkle present in the suspended drum, creating two resonance frequencies for certain amounts of strain in the drum. After the 10 V, the drum is most likely streched to a point where the wrinkle is flattened, showing one resonance peak (like samples without wrinkles). So although this sample shows the largest tunability range and highest tuning sensitivity, it is difficult to recreate this kind of device and perform accurate measurements, as the presence of the wrinkle on the drum was an accident and can not be controlled in a way that provides predictable results in measurements.

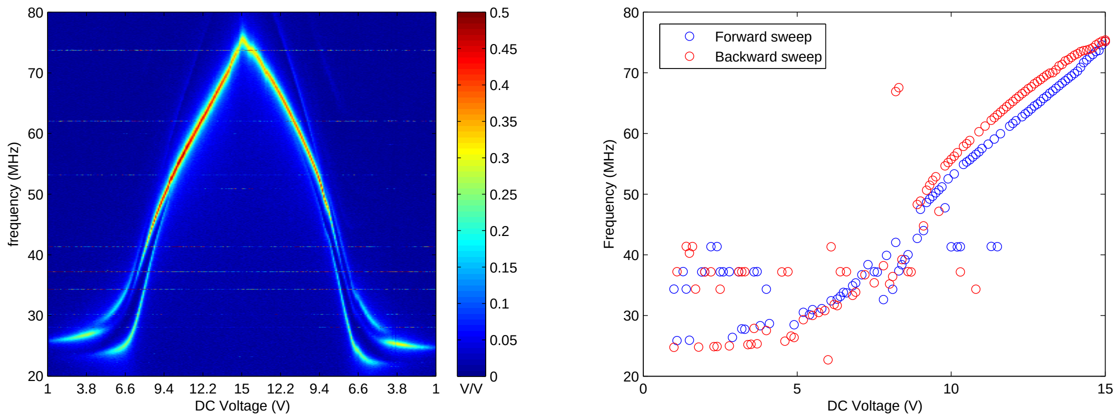

(a) (b)

Figure 4.3.3: Figure 4.3.3a shows large tuning data of sample E and figure 4.3.3b is a plot of the fitted resonance frequencies of that data. The large tuning shows resonance frequencies increasing from 25 MHz to 75 MHz for DC voltages going from 1 V to 15 V.

There are other samples that show both negative and positive frequency tuning. The DC voltage until which negative tuning occurs is again dependent on the built-in strain. Firstly, sample B showed negative tuning when applying DC voltages up to 5 V. This is shown in figure 4.3.4.

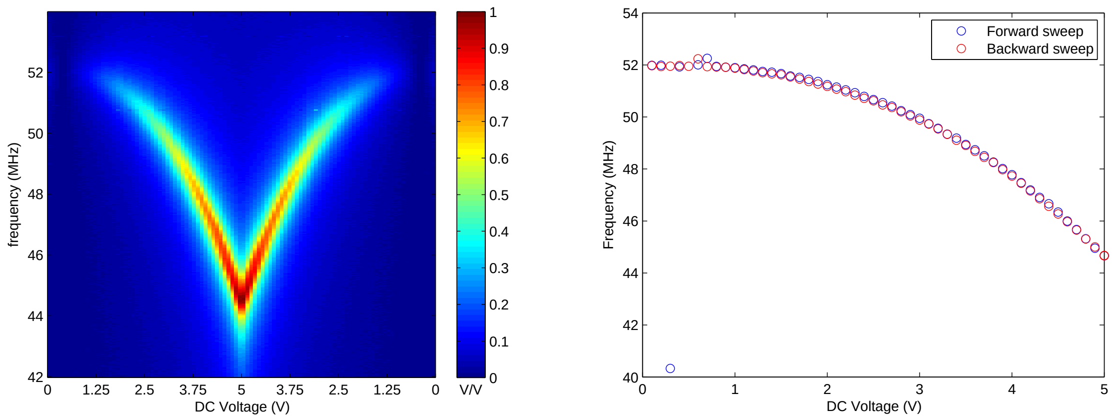

(a) (b)

Figure 4.3.4: The magnitude data in figure 4.3.4a shows data of sample B and figure 4.3.4b is a plot of the fitted resonance frequencies of that data. The negative tuning occurs during the entire DC voltage range of 0 - 5 V.

The frequency tuning is largest between 4 V and 5 V, where this measurement shows a frequency tuning of 3.1 MHz/V. Note that this is the maximum frequency tuning. When calculating the amount of tuning between 2 V and 3 V, values around 0.5 MHz/V are found.

When the voltage is increased enough, the electrostatic spring weakening is not sufficient to continue the negative frequency tuning and the induced strain causes positive frequency tuning. The same sample was measured with a DC voltage range of 0 - 10 V and it became obvious there was a transition at 8 V. However, these results should not be used to draw any conclusions, since the drum starts to transition into the non-linear resonance regime around 6 V. Therefore, the SHO model does not fit to the data any more and there is no accurate data on the resonance frequency and Q-factors. Modeling the nonlinear behaviour of electrically driven resonators is as said before outside the scope of this thesis.

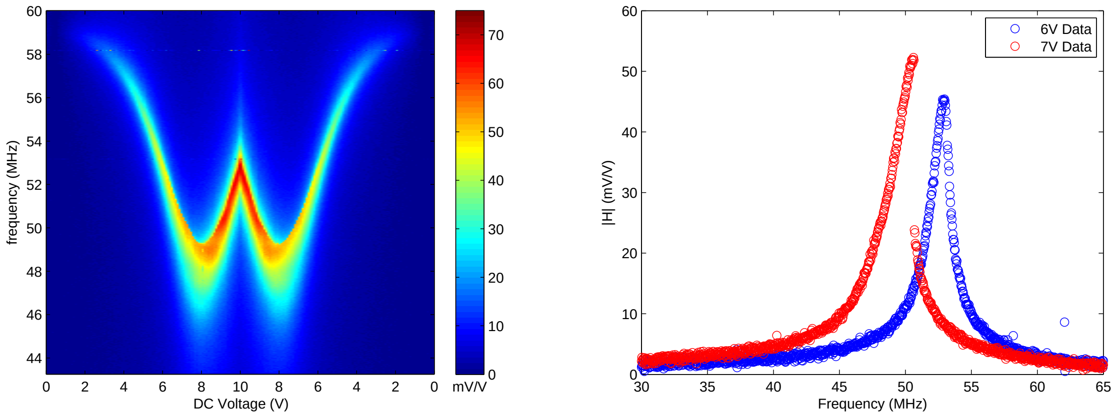

(a) (b)

Figure 4.3.5: The magnitude data in figure 4.3.5a shows data of sample B and figure 4.3.4b is a plot of two specific DC voltages. The negative tuning occurs during the entire DC voltage range of 0 - 8 V, after which the tuning starts to become positive. However, as can be seen in the magnitude plot at the DC voltages around the switch from negative to positive frequency tuning, the resonance becomes nonlinear at this point (a line trace for specific frequencies around 8 V show a nonsymmetric shape). It is defined clearly in the seperate traces at DC voltages, where the frequency spectra with applied DC voltages of 6 V and 7 V are plotted seperately. The blue trace (6 V) shows the first indication the peak becomes nonsymmetric and the red trace (7 V) clearly indicates nonlinear behaviour.

Even though this set of data can strictly not be used to determine the frequency tuning sensitivity, when fitting frequency spectra for specific ranges of DC voltages which do show linear behaviour, an estimate of the tuning sensitivity can still be made. The negative frequency tuning in sample B is calculated and the maximum value, measured between 5.5 V and 6 V DC voltage is 2.65 MHz/V. The positive tuning (measured between 9.5 V and 10 V) is 3.13 MHz/V.

Finally, data obtained from sample C are processed. This sample was tested by applying a DC voltage starting at 0 V, then decrease to a certain voltage, say -10 V, after that increased up to 10 V and finally back to 0 V. Sample C is by far the thickest sample measured, but also shows the most promising frequency tuning response. Figure 4.3.6 shows the magnitude data and fitted resonance frequencies of the data.

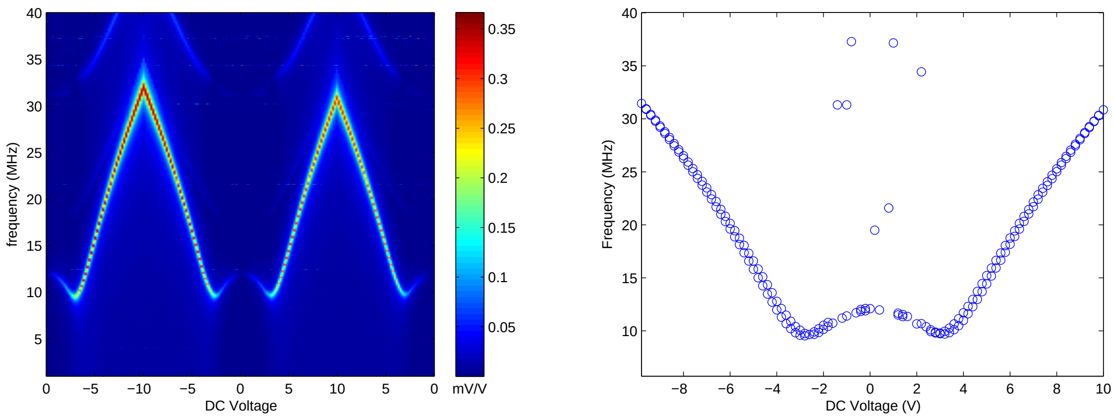

(a) (b)

Figure 4.3.6: The magnitude data in figure 4.3.6a shows data of sample C and figure 4.3.6b is a plot of the fitted resonance frequencies.

Due to the small negative frequency tuning (from 12.1 MHz at 0 V to 9.54 MHz at -2.8 V), only the positive frequency tuning sensitivity in this sample is calculated. The tunability range for this dataset is 22.4 MHz over 10 V. However negative tuning occurs between -2.8 V and 2.8 V. The 22.4 MHz resonance frequency increase occurs at negative voltages (this profile is not entirely symmetrical around 0 V, it is symmetrical around 0.3

V), meaning this tunability is caused by a decrease in DC voltage of 7.2 V. The frequency tuning sensitivity is therefore the highest found in any sample, 7.62 MHz/V. This means that the 8 MHz/V sensitivity observed by Chen *et al.* [12] has been approached within 5%. Note that the improved sample fabrication method as explained in section 3.1.3 was used on samples with a 50 nm silicon dioxide gap, a 5 nm Chromium layer and a 90 nm Gold-Palladium layer for a total gap of 145 nm between the drum and gate. The sample that achieved the 8 MHz/V tuning sensitivity in [12] has a 200 nm gap between drum and gate, which should cause a slightly worse capacitive coupling. This means it should be possible to improve upon the 7.62 MHz/V achieved during this project.

4.3.3. FITTING THE DATA TO THE FREQUENCY TUNING MODEL

The next step is to test whether the results that were obtained during measurements fit the model proposed by Chen [37]. Most important is the amount of positive and negative frequency tuning as a function of DC voltage, which according to Chen depends on two parameters, the built-in strain and the effective mass. These two parameters and the DC voltage are present in three terms, α, β and γ as shown in equation 2.24. They are combined in equation 2.23 to calculate the equilibrium position of a suspended drum for each DC voltage. The resonance frequency is then iteratively calculated as a function of DC voltage. This iteration process makes it difficult to create an automatic fitting tool to acquire the two fitting parameters ε_0, the built-in strain, and m_{eff}, the effective mass. Therefore, through trial and error, estimations have been made about these parameters to acquire a plot of the model that fits the measurement results. Figure 4.3.8 shows how the model and the measurement overlap in some areas, but do not fit very well. The measurements from sample C are shown here, which is the same data as figure 4.3.6.

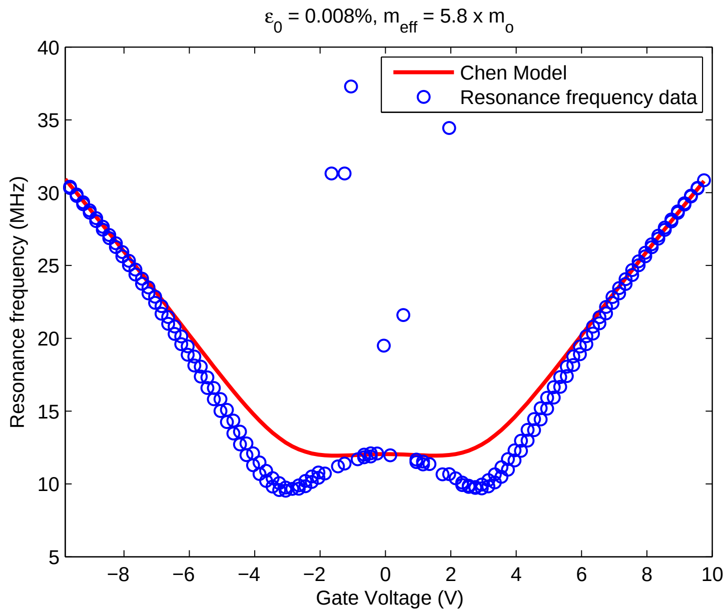

Figure 4.3.7: The data of sample C, shown in figure 4.3.6 is fitted with the proposed model by Chen [37]. A build-in strain of 0.008 % and an effective mass of 5.8 times the mass of the MoS_2 drum are used to obtain this plot of the model.

Unfortunately, the model does not fit the measurement very well. Other values for $\varepsilon_0 and m_0$ have been tried, but they do not yield better results. The biggest difference between the measurement and model in this case is the amount of negative frequency tuning. The measurement clearly shows a tuning that decreases the resonance frequency by several MHz when applying DC voltages between -2.8 V and 2.8 V. The model does not allow this amount of negative frequency tuning. The proposed model does have the assumption build in it that there is no bending rigidity in the drum, because it is assumed to be a drum and not a plate. However, specifically for sample C, the frequency spectrum seems to indicate that this device is a plate and not a membrane, because the second resonator mode appears at approximately twice the frequency of the fundamental mode. According to Wah [38], this property indicates the device is a plate and its behaviour is dominated by its bending rigidity and not its build-in tension. Therefore, bending rigidity can certainly not be neglected. Simply adding a bending rigidity term in the model by Chen does not show any improvement in fitting the measurement to the theory, so a more extensive model is required to incorporate the bending rigidity. This could more accurately describe the behaviour of a plate which is deformed due to an electrostatic force.

In order to check the model without additional bending rigidity, measurement results of other samples are tested to fit the model.

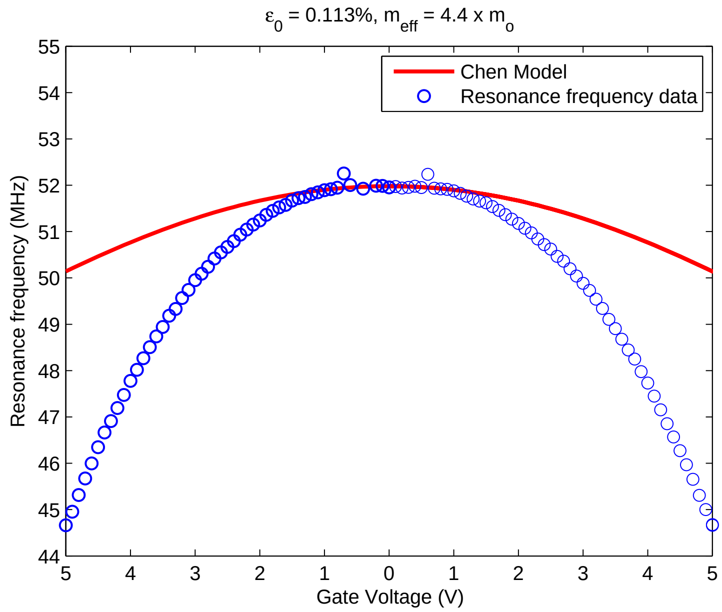

Figure 4.3.8: The data of sample B, shown in figure 4.3.4b is fitted with the proposed model by Chen. A build-in strain of 0.113 % and an effective mass of 4.4 times the mass of the MoS_2 drum are used to obtain this plot of the model.

As is once again concluded, the amount of negative frequency tuning is not comparable to that possible in the model. The data presented in Chen's papers [12, 37] does not show any negative frequency tuning ranges of sensitivities with similar values, so the results obtained in this thesis also do not compare to previous measurements. The only results that were found to be similar were achieved by Song *et al.* [39] for rectangular graphene sheets. They use the theory developed by Sapmaz *et al.* [40] for carbon nanotubes and later experimentally shown by Chen *et al.*, also for rectangular graphene sheets [8].

When fitting the positive tuning results, the measurements of sample A are analysed. Sample A showed positive frequency tuning (visible in figure 4.2.3), but has a very low frequency tuning sensitivity of 0.44 MHz/V. The initial resonance frequency, without an applied DC voltage, is 48.3 MHz, which is higher than most other measured samples. The low sensitivity causes enormous difficulties when trying to obtain fitting parameters for this measurement as low sensitivities mostly occur at lower resonance frequencies. To acquire equal tuning sensitivities, there is always negative frequency tuning at lower DC voltages before positive frequency tuning occurs. Fitting parameters are adjusted to unrealistic values to obtain similar tuning sensitivity curves, especially with an effective mass of 600 times the mass of the graphene drum. Still, the resonance frequencies are 46 MHz too low, but the behaviour does correspond.

The fitting parameter values of $m_{eff} = 600 * m_0$ and $\varepsilon_0 = 0,02\%$ that are used to create figure 4.3.9 are absurd and are not expected to be the actual values of the build-in strain and effective mass of this sample. Especially the effective mass is out of proportion with 600 times the initial mass. The effective mass is often used to correct the spring constant for fluctuating membranes between values of 0.5 and 2 times the initial mass. Using it as a fitting parameter in the Chen model could provide information about each sample, as these parameters are different for each sample due to the stamping method used during this thesis. However, these values show that the model does not provide a clear explanation of the results acquired in experiments. Unfortunately no theoretical model has been found to explain the behaviour of the different drums yet, because even though the dimensions are similar in each device, the behaviour does seem to strongly depend on the initial parameters of the stamped drums.

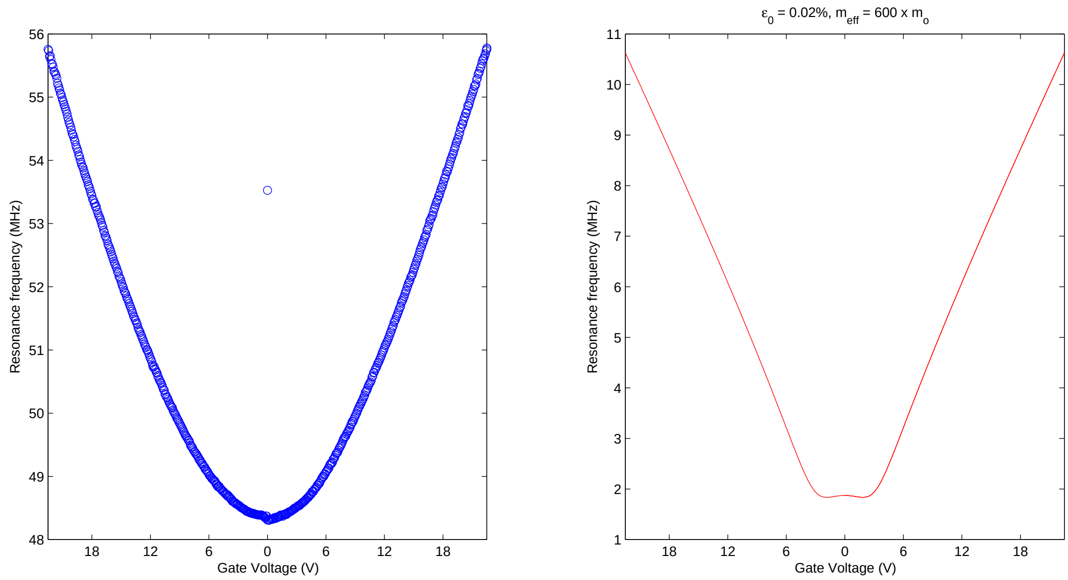

Figure 4.3.9: The data of sample A, shown in figure 4.2.3 shows similar frequency tuning sensitivities as in the model by Chen [37]. A build-in strain of 0.02 % and an effective mass of 600 times the mass of the graphene drum are used to obtain this plot of the model in order to obtain the low tuning sensitivity as shown in the data. However, these fitting parameters have unrealisitic values and do not even provide the correct resonance frequency.

A final note about obtained results is the fact that measured resonance frequencies and frequency tuning behaviours appeared to change over time or over several measurements. A prime example of this change is seen in the measurements of sample C. The frequency tuning behaviour as a function of DC voltage is shown in figure 4.3.8 and show negative tuning for low voltages and positive tuning for higher voltages (below -2.8 V and above +2.8 V). However, after several measurements (11 frequency tuning measurements), the negative frequency tuning dissapeared.

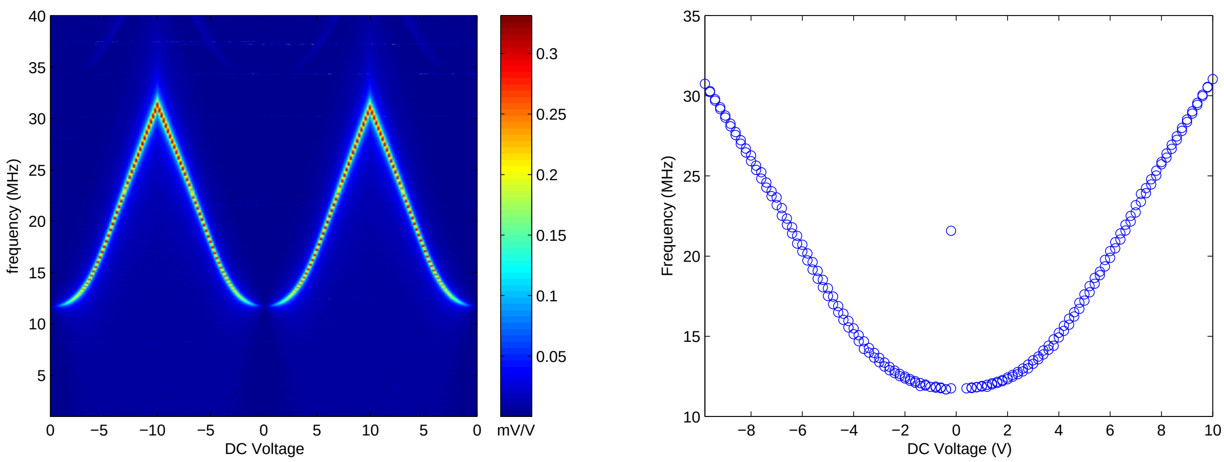

(a) (b)

Figure 4.3.10: The magnitude data in figure 4.3.10a shows data of sample C and figure 4.3.10b is a plot of the fitted resonance frequencies. Note how this data does not show negative frequency tuning, while it is the sample sample as figure 4.3.6.

As can be seen in figure 4.3.10, the negative tuning that occurred between -2.8 V and +2.8 V has dissapeared and only positive frequency tuning is present. Any following measurements showed the same result. Although unverified, the most likely explanation is that due to streching the membrane multiple times when measuring the frequency tuning, tension is build up in the membrane, changing the initial conditions for each measurement, because more initial tension would cause the electrostatic spring softening of the spring constant to have less effect on the resonance frequency.

Other samples did not show such a dramatic change in behaviour, but other changes did occur. For instance, over time slightly different resonance frequencies when all conditions (sample, measured drum, pressure, actuation method and actuation power) were kept constant. A possible explanation for a change in resonance frequency could be due to slight drift in the sample, which would cause the position of the drum which is measured to be changed somewhat, which could affect the measurement. However, many consistent results were obtained as well, on which the calculations and conclusions in this chapter are based.

5 CONCLUSIONS AND OUTLOOK

5.1. CONCLUSIONS

When starting this thesis, the main goal was to electrically actuate membranes in the current interferometer setup. As can be concluded from the results in section 4.1, this was found to be easily implemented. Experiments were done to compare the resonance frequency and quality factors of drum actuated with the two different actuation methods, electrical drive and optical drive. These were found to be very similar. Resonance frequencies of 21.3 MHz and a quality factor of 73.5 found when driving optically for the initial sample are almost equal to the 19.9 MHz resonance frequency and 85.7 quality factor that were obtained in the electrically driven resonance. The biggest difference between the two actuation methods was the magnitude of the resonance frequency signal, which was a factor 100 larger for optical actuation than the signal seen with electrical actuation.

Frequency tuning by combining the electrical actuation with a DC voltage was also succesful with the initial sample. The frequency tuning was observed to decrease when applying a positive DC voltage. However, many difficulties arose when performing multiple measurements. High DC voltages provided unstable and unreproducable results and a large hysteresis in resonance frequency as a function of DC voltage was found for all voltages. Most likely this occured due to charging of the sample due to two parasitic capacitances: one between the electrode (the top chromium layer) and the back gate (the silicon sample) and the second between the electrode and the flake of graphene, causing a floating device.

Taking the results of the initial sample in mind, a fabrication method was succesfully developed to create substrates to provide more reproducable results. A reduced electrode area achieved with a different design and using a gold palladium electrode in stead of the chromium layer are the most important changes. No hysteresis was found in any drums made of flakes stamped on these new substrates. Tuning the frequency with both positive and negative DC voltages provided consist results and even when taking DC voltage steps of 1 V in stead of 0.1 V for each measurement, the resonance frequency response remained the same.

A closer look was taken at the frequency tuning. The amplitude of the frequency signal for electrical actuation was investigated, which was already found to increase for increasing DC voltages in the initial sample. All other samples made show the same effect. When keeping the RF modulated actuation voltage constant and sweeping up from 0 V to any positive DC voltage and from 0 V down to any negative DC voltage, an increase in amplitude is observed. At low DC voltages, amplitudes of tens of mV/V are seen, while higher DC voltages increase to several hundreds of mV/V. However, amplitudes remain reasonably constant when actuating optically, thus the increase in amplitude seen when actuating electrically and applying DC voltages has to be a combination of the two voltages applied. There does not seem to be a linear relation between the amplitude and the applied DC voltage, there are several regimes in which the amplitude increases differently. There is no explanaition found for this phenoma yet.

Furthermore, the resonance frequency tuning range was calculated for both positive and negative frequency tuning (respectively increasing and decreasing resonance frequencies for increasing DC voltages). By dividing the tunability range by the DC voltage range that was used to tune, the more interesting tuning sensitivity is calculated, which was compared to values found in literature. These values fluctuate from 0.44 MHz/V to 7.62 MHz/V at room temperature in the fabricated devices. The 7.62 MHz/V achieved is within 5 % of the maximum value of 8 MHz/V found by Chen *et al.* [12].

Finally, the frequency tuning curves were fitted to the model described in the theory, but the two free parameters build-in strain ε_0 and effective mass m_0 do not provide realistic values when trying to fit the acquired data from measurements to the model. A more thorough analysis of the affect the fabrication method has on the mechanical properties (more specifically the resonance frequency) of the devices is needed in order to more productively model the behaviour of electrically actuated 2D membranes.

5.2. OUTLOOK

To implement the electrical actuation into future experiments, the devices that can be created need to consistently provide the same results, which is still somewhat of a difficulty. Due to the fabrication method, there will always be some variation in the devices, such as membrane thickness and build-in strain. The main unsolved problem in this thesis is fitting the obtained data to a model. However, developing this model is only required for further investigation of the frequency tuning possibilities of 2D membranes.

One interesting conclusion from this thesis is the change in amplitude when actuating electrically and tuning the frequency with a DC voltage. The increase in amplitude is proposed to occur due to an increase in actuation power, which depends on the product of the RF voltage and DC voltage. Even though the amplitude plots do not show linear behaviour as a function of DC voltage, a simple experiment could be done with devices fabricated as in this thesis to test this hypothesis. A control program can easily be written to regulate both the RF voltage and the DC voltage that are applied in order to do the frequency tuning measurements and keeping the product of the RF voltage and DC voltage constant. This would provide more insight into the dependence of the amplitude on the electrical actuation and whether this is something to take into account. A deeper insight into the complete amplitude behaviour could be to investigate the higher vibrational modes of the membranes and their amplitudes, as for instance a second mode amplitude should not be affected by a membrane deflection due to a DC voltage.

A possible use for the increase in amplitude is when using the gate coupling of the device to create a feedback system where amplitude of a membrane is measured and fed back as an actuation signal. Applying a DC voltage appears to amplify this effect, so it can be used to locate weak resonance frequency signals. Feedback would be used more effectively if both actuation and read-out could happen electrically, to remove the noise component of all optical elements in the setup.

The electrical actuation can already be used as a replacement for the optical actuation in experiments that investigate physical phenomena that are dependent on temperature.

If the behaviour of the resonance frequency of can be succesfully modelled, this model could be used to characterize the free parameters (assumed to be the build-in tension and effective mass) in devices.

Future development of the devices could include local actuation of more complex geometries, such as dumbells or trenches to determine the transport of energy through 2D materials by measuring the resonance frequency and quality factor at multiple positions in a membrane.

BIBLIOGRAPHY

[1] G. E. Moore *et al.*, *Cramming more components onto integrated circuits, 1965,* Electronics Magazine , 4 (1965).

[2] K. S. Novoselov, A. K. Geim, S. Morozov, D. Jiang, Y. Zhang, S. Dubonos, I. Grigorieva, and A. Firsov, *Electric field effect in atomically thin carbon films,* science **306**, 666 (2004).

[3] K. Novoselov, A. K. Geim, S. Morozov, D. Jiang, M. K. I. Grigorieva, S. Dubonos, and A. Firsov, *Two-dimensional gas of massless dirac fermions in graphene,* nature **438**, 197 (2005).

[4] A. K. Geim and K. S. Novoselov, *The rise of graphene,* Nature materials **6**, 183 (2007).

[5] J. S. Bunch, A. M. Van Der Zande, S. S. Verbridge, I. W. Frank, D. M. Tanenbaum, J. M. Parpia, H. G. Craighead, and P. L. McEuen, *Electromechanical resonators from graphene sheets,* Science **315**, 490 (2007).

[6] J. S. Bunch, *Mechanical and electrical properties of graphene sheets* (Cornell University, 2008).

[7] A. K. Geim, *Graphene: status and prospects,* science **324**, 1530 (2009).

[8] C. Chen, S. Rosenblatt, K. I. Bolotin, W. Kalb, P. Kim, I. Kymissis, H. L. Stormer, T. F. Heinz, and J. Hone, *Performance of monolayer graphene nanomechanical resonators with electrical readout,* Nature nanotechnology **4**, 861 (2009).

[9] A. Castellanos-Gomez, N. Agraït, and G. Rubio-Bollinger, *Optical identification of atomically thin dichalcogenide crystals,* Applied Physics Letters **96**, 213116 (2010).

[10] A. Castellanos-Gomez, M. Poot, G. A. Steele, H. S. van der Zant, N. Agraït, and G. Rubio-Bollinger, *Elastic properties of freely suspended mos2 nanosheets,* Advanced Materials **24**, 772 (2012).

[11] A. Castellanos-Gomez, M. Poot, G. A. Steele, H. S. van der Zant, N. Agraït, and G. Rubio-Bollinger, *Mechanical properties of freely suspended semiconducting graphene-like layers based on mos2,* Nanoscale research letters **7**, 1 (2012).

[12] C. Chen, S. Lee, V. V. Deshpande, G.-H. Lee, M. Lekas, K. Shepard, and J. Hone, *Graphene mechanical oscillators with tunable frequency,* Nature nanotechnology **8**, 923 (2013).

[13] A. Castellanos-Gomez, R. van Leeuwen, M. Buscema, H. S. van der Zant, G. A. Steele, and W. J. Venstra, *Single-layer mos2 mechanical resonators,* Advanced Materials **25**, 6719 (2013).

[14] F. Bonaccorso, Z. Sun, T. Hasan, and A. Ferrari, *Graphene photonics and optoelectronics,* Nature photonics **4**, 611 (2010).

[15] R. A. Barton, I. R. Storch, V. P. Adiga, R. Sakakibara, B. R. Cipriany, B. Ilic, S. P. Wang, P. Ong, P. L. McEuen, J. M. Parpia, *et al.*, *Photothermal self-oscillation and laser cooling of graphene optomechanical systems,* Nano letters **12**, 4681 (2012).

[16] V. Singh, S. Bosman, B. Schneider, Y. Blanter, A. Castellanos-Gomez, and G. Steele, *Optomechanical coupling between a graphene mechanical resonator and a superconducting microwave cavity,* arXiv preprint arXiv:1403.5165 (2014).

[17] A. C. Neto, F. Guinea, N. Peres, K. S. Novoselov, and A. K. Geim, *The electronic properties of graphene,* Reviews of modern physics **81**, 109 (2009).

[18] Q. H. Wang, K. Kalantar-Zadeh, A. Kis, J. N. Coleman, and M. S. Strano, *Electronics and optoelectronics of two-dimensional transition metal dichalcogenides,* Nature nanotechnology **7**, 699 (2012).

[19] I. Frank, D. M. Tanenbaum, A. Van der Zande, and P. L. McEuen, *Mechanical properties of suspended graphene sheets,* Journal of Vacuum Science & Technology B **25**, 2558 (2007).

[20] C. Lee, X. Wei, J. W. Kysar, and J. Hone, *Measurement of the elastic properties and intrinsic strength of monolayer graphene,* science **321**, 385 (2008).

[21] A. Bosseboeuf and S. Petitgrand, *Application of microscopic interferometry techniques in the mems field,* in *Optical Metrology* (International Society for Optics and Photonics, 2003) pp. 1–16.

[22] B. Ilic, S. Krylov, K. Aubin, R. Reichenbach, and H. Craighead, *Optical excitation of nanoelectromechanical oscillators,* Applied Physics Letters **86**, 193114 (2005).

[23] W. C. Tang, T.-C. H. Nguyen, M. W. Judy, and R. T. Howe, *Electrostatic-comb drive of lateral polysilicon resonators,* Sensors and Actuators A: Physical **21**, 328 (1990).

[24] V. Sazonova, Y. Yaish, H. Üstünel, D. Roundy, T. A. Arias, and P. L. McEuen, *A tunable carbon nanotube electromechanical oscillator,* Nature **431**, 284 (2004).

[25] K. Ekinci, Y. Yang, X. Huang, and M. Roukes, *Balanced electronic detection of displacement in nanoelectromechanical systems,* Applied physics letters **81**, 2253 (2002).

[26] X. M. H. Huang, C. A. Zorman, M. Mehregany, and M. L. Roukes, *Nanoelectromechanical systems: Nanodevice motion at microwave frequencies,* Nature **421**, 496 (2003).

[27] J. Soderkvist and K. Hjort, *The piezoelectric effect of gaas used for resonators and resonant sensors,* Journal of Micromechanics and Microengineering **4**, 28 (1994).

[28] S. C. Masmanidis, R. B. Karabalin, I. De Vlaminck, G. Borghs, M. R. Freeman, and M. L. Roukes, *Multifunctional nanomechanical systems via tunably coupled piezoelectric actuation,* Science **317**, 780 (2007).

[29] M. Tortonese, R. Barrett, and C. Quate, *Atomic resolution with an atomic force microscope using piezoresistive detection,* Applied physics letters **62**, 834 (1993).

[30] I. Bargatin, E. Myers, J. Arlett, B. Gudlewski, and M. Roukes, *Sensitive detection of nanomechanical motion using piezoresistive signal downmixing,* Applied Physics Letters **86**, 133109 (2005).

[31] T. B. Jones and N. G. Nenadic, *Electromechanics and MEMS* (Cambridge University Press, 2013).

[32] L. D. Landau and E. Lifshitz, *Theory of elasticity, vol. 7,* Course of Theoretical Physics **3** (1986).

[33] S. Timoshenko, S. Woinowsky-Krieger, and S. Woinowsky-Krieger, *Theory of plates and shells*, Vol. 2 (McGraw-hill New York, 1959).

[34] A. Castellanos-Gomez, M. Buscema, R. Molenaar, V. Singh, L. Janssen, H. S. van der Zant, and G. A. Steele, *Deterministic transfer of two-dimensional materials by all-dry viscoelastic stamping,* 2D Materials **1**, 011002 (2014).

[35] J. de Koning, *Physics of compound nanodrums,* (2013).

[36] V. Adiga, R. De Alba, I. Storch, P. Yu, B. Ilic, R. Barton, S. Lee, J. Hone, P. McEuen, J. Parpia, *et al.*, *Simultaneous electrical and optical readout of graphene-coated high q silicon nitride resonators,* Applied Physics Letters **103**, 143103 (2013).

[37] C. Chen, *Graphene NanoElectroMechanical Resonators and Oscillators* (2013).

[38] T. Wah, *Vibration of circular plates,* the Journal of the Acoustical Society of America **34**, 275 (1962).

[39] X. Song, M. Oksanen, M. A. Sillanpaa, H. Craighead, J. Parpia, and P. J. Hakonen, *Stamp transferred suspended graphene mechanical resonators for radio frequency electrical readout,* Nano letters **12**, 198 (2011).

[40] S. Sapmaz, Y. M. Blanter, L. Gurevich, and H. Van der Zant, *Carbon nanotubes as nanoelectromechanical systems,* Physical Review B **67**, 235414 (2003).